

1 **Cover Letter**

2 Bologna, May 5<sup>th</sup> 2019

3

4

5 Dear editor,

6

7 we herewith submit to your attention the revised version of our manuscript "**Fluid-mediated, brittle-ductile deformation**  
8 **at seismogenic depth: Part I – Fluid record and deformation history of fault-veins in a nuclear waste repository**  
9 **(Olkiluoto Island, Finland)**", hoping that you will find it improved toward its publication in Solid Earth. As you know,  
10 the open discussion has been a very fruitful and constructive process, which has greatly helped us to sharpen our work and  
11 improve it in light of some constructive criticisms that were made by the three reviewers.

12 Our detail rebuttals to each of them were already prepared and a point-by-point reply was prepared to the purpose of the  
13 open discussion. In that occasion we discussed openly each point made and explained how we would implement the  
14 required changes in the final, amended version.

15 We have now done it and there is no point for us to repeat all the content of the initial rebuttals. We confirm here that we  
16 changed the manuscript and the figures as per discussion, doing exactly what we said we would do.

17 To help you appreciate the revision work, we submit a version of the file in review mode, with all changes highlighted.  
18 Please note that all minor comments and requests of changes were basically taken care of in the final version.

19 To sum up our revision work, we can repeat here the main changes:

20 -We have tried to shorten and streamline the manuscript by polishing the language and removing unnecessary text sections  
21 and even some repetitions.

22 -We have modified some of the figures to comply with the request of one reviewer. We have prepared a Supplementary  
23 Material section with some extra data, figures and information.

24 -We have acquired extra EBSD data to better support our interpretation of some unclear microstructures of Qtz I.

25 -We have acquired extra FI data to strengthen the analysis of the fluids involved during deformation. This has brought us  
26 to a more open discussion as to the number and chemical composition of the fluid batches that ingressed the fault during  
27 its evolution.

28 -After the second reviewer comments, we added to the new version of Figure 12 hydrostatic and lithostatic pressures,  
29 reconstructed in accordance with regional gradients at the time of vein emplacement. These gradients are used to constrain the  
30 upper and lower bounds to physically possible fluid pressure values.

31 -We added the chlorite compositional diagram on Figure 11 with the aim to argue about the composition of the fluid  
32 batches.

33 -In accordance with the first reviewer, we have shorten the Abstract.

34 -We also added to the main text most of the bibliography suggested by the reviewers.

35

36 Please address all the correspondence to:

37

38 Barbara Marchesini

39 PhD Student

40 Department of Biological, Geological, and Environmental Sciences (Bi.Ge.A.)

41 University of Bologna

42 Via Zamboni, 67, I-40126 Bologna.

43 E-mail: [barbara.marchesini2@unibo.it](mailto:barbara.marchesini2@unibo.it).

44

45 We look forward to hearing from you at your earliest convenience.

46

47 Best regards,

48 Barbara Marchesini, corresponding author.

49

50

51

52

53

54

55

56

57

58

59

60

61

62

63 **Fluid-mediated, brittle-ductile deformation at seismogenic depth:**  
64 **Part I- Fluid record and deformation history of fault-veins in a**  
65 **nuclear waste repository (Olkiluoto Island, Finland)**

66  
67 Barbara Marchesini<sup>1§</sup>, Paolo Stefano Garofalo<sup>1</sup>, Luca Menegon<sup>2</sup>, Jussi Mattila<sup>3</sup> and Giulio Viola<sup>1</sup>

68  
69 <sup>1</sup>Dipartimento di Scienze Biologiche, Geologiche e Ambientali, Università di Bologna, Italy

70 <sup>2</sup>School of Geography, Earth and Environmental Sciences, University of Plymouth, PL48AA Plymouth, UK

71 <sup>3</sup>Geological Survey of Finland (GTK), Espoo, Finland

72 <sup>§</sup>Correspondence to: [barbara.marchesini2@unibo.it](mailto:barbara.marchesini2@unibo.it)

73

74 **Abstract.** The dynamic evolution of fault zones at the seismogenic brittle-ductile transition zone (BDTZ) expresses the delicate  
75 interplay of ~~between~~ numerous physical and chemical processes ~~that occur at the time of strain localization~~. Deformation and  
76 ~~fluid flow of aqueous fluids within these zones, in particular, at the BDTZ~~ are closely related and mutually dependent during  
77 ~~repeating and transient cycles of repeating, transient~~ frictional and viscous deformation. Despite numerous studies documenting  
78 in detail seismogenic faults exhumed from the BDTZ, uncertainties remain as to the ~~exact~~ role of fluids in facilitating ~~broadly~~  
79 ~~coeval brittle and ductile~~ deformation ~~at that structural level in this zone, particularly with regard to the mechanics of broadly~~  
80 ~~coeval brittle and ductile deformation~~. We combine ~~here~~ structural analysis, fluid inclusion ~~data~~ and mineral chemistry data from  
81 synkinematic and authigenic minerals to reconstruct the temporal variations in ~~fluid pressure (P), temperature (T), and bulk~~  
82 composition (X) of the fluids that mediated deformation and steered strain localization ~~in along BFZ300, a strike-slip fault from~~  
83 ~~originally active at the BDTZ. This is a fault formed within BFZ300 deforms~~ the Paleoproterozoic migmatitic basement of  
84 southwestern Finland ~~and, hosting-hosts~~ in its core two laterally continuous quartz veins formed by two texturally distinct ~~types~~  
85 of quartz ~~types~~ – Qtz I and Qtz II, ~~where with Qtz I is demonstrably older than Qtz II~~. Veins within the ~~diffuse~~ damage zone of  
86 ~~the fault~~ are ~~formed~~ ~~in~~ ~~filled~~ exclusively by Qtz I. ~~Meso- and microstructural Multi-scalar structural analysis combined with fluid~~  
87 ~~geochemistry compositional data~~ indicate ~~s~~ recurrent cycles of mutually overprinting brittle and ductile deformation ~~triggered by~~  
88 ~~fluid pressure oscillations of fluid pressure, with documented peaking at pressure of 210 MPa~~. Fluid inclusion microthermometry  
89 and mineral pair geothermometry indicate that ~~both the two documented quartz types precipitated from a distinct different fluid~~  
90 ~~batches phases, that was in a homogeneous state during the recurrent cycles of faulting, and whose with bulk salinities were~~ was  
91 ~~at first in the 1-50-5 wt% NaCl<sub>eq</sub> range for Qtz I and then evolved in in the 6-11 wt% NaCl<sub>eq</sub> range for Qtz II, for Qtz I and Qtz~~  
92 ~~II respectively~~. The temperature of the fluids ~~phases~~ involved with the various episodes of initial strain localization and later ~~fault~~  
93 reactivation ~~changed with time evolved through time, from >e. 350 °C or even higher temperature 240 °C in the damage zone to~~  
94 ~~e. 350 °C in the core~~ during Qtz I precipitation to < ~~3200~~ °C at the time of Qtz II crystallization. ~~P~~ ~~The peak values of P~~ fluid  
95 pressure estimates ~~show constrain an oscillation pore pressure oscillations in pore pressure comprised between 80 and -210460~~

Formattato: Colore carattere: Testo 1

Formattato: Colore carattere: Testo 1

Formattato: Colore carattere: Testo 1

Formattato: Colore carattere: Testo 1

Formattato: Colore carattere: Testo 1

Formattato: Colore carattere: Testo 1

Formattato: Colore carattere: Testo 1, Non Apice / Pedice

Formattato: Colore carattere: Testo 1

Formattato: Colore carattere: Testo 1

Formattato: Colore carattere: Testo 1

Formattato: Colore carattere: Testo 1

Formattato: Colore carattere: Testo 1

Formattato: Colore carattere: Testo 1

Formattato: Colore carattere: Testo 1

Formattato: Colore carattere: Testo 1

Formattato: Colore carattere: Testo 1

Formattato: Colore carattere: Testo 1

Formattato: Colore carattere: Testo 1

Formattato: Colore carattere: Testo 1

Formattato: Colore carattere: Testo 1

Formattato: Colore carattere: Testo 1

96 and 10 MPa during the ~~several recorded documented~~ fault-activitying stages/episodes. Our results suggest significant variability in  
97 of the overall physical-chemical conditions of the fluids steering deformation phase ( $P_i$ ,  $T_i$ ,  $P_f$ ,  $X$ )-reflecting during the fault  
98 deformation history, reflecting the ingress and interaction effects of several multiple batches of different fluid compositions fluid  
99 possibly reflecting the interaction of several batches of compositionally similar fluids ingressing in the dilatant fault zone at  
100 different stages of its evolution, each with specific  $T$  and  $P_i$  conditions. Initial, fluid-mediated embrittlement of the faulted rock  
101 volume generated a diffuse network of joints and/or hybrid/shear fractures in the damage zone, whereas, progressive subsequent  
102 strain localization led to more localized deformation within the fault core. Localization was guided by cyclically increasing fluid  
103 pressure and transient embrittlement of a system that was otherwise at under overall ductile conditions.  
104 Our analysis implies/suggests that fluid overpressure at the brittle-ductile transition BDTZ can play a key role in the initial  
105 embrittlement of the metamorphic basement deforming rock and steer subsequent strain localization mechanisms.

106

## 107 1 Introduction

108 The physical and chemical properties of fault systems play a fundamental role in controlling the rheological behaviour of the  
109 Earth's crust and in steering channelled fluid flow (e.g. Caine et al., 1996). Deformation and fluid flow are closely related and  
110 mutually dependent via a number of feedbacks, such as the control that fluids exert upon the effectiveness of deformation  
111 processes and the development of fault systems at all scales, and the control by rock heterogeneities and/or fracture system  
112 topology on the net fault transmissivity (e.g. Crider and Peacock, 2004). The nucleation and development of permeable fault  
113 systems and the mechanisms whereby individual faults may weaken and eventually fail are, therefore, complex functions of a  
114 number of processes. In this perspective, the multiscale interaction between fluid and mineral phases within fault rocks needs to  
115 be studied with a system approach in order to single-out the roles and importance of all processes involved (Kaduri et al., 2017).  
116 The most evident An obvious effect of fluid involvement, particularly in crustal volumes that have experienced large deformation-  
117 controlled fluid fluxes, is the precipitation of authigenic and hydrothermal minerals within faults (Oliver and Bons, 2001; Viola  
118 et al., 2016) and their immediately adjacent host rock (Mancktelow and Pennacchioni, 2005; Garofalo, 2004). In the seismogenic  
119 region of the crust, where fluids may even be the primary driver of the seismic cycle (e.g. Miller, 2013), faults have been shown  
120 to have the potential to function like a "fluid-activated valve", whereby they experience transient and cyclic fluid pressure build-  
121 up before sudden fluid venting, pore pressure- and mechanical strength drop concomitant with seismic failure (e.g. Sibson, 1989,  
122 1992b, 1993; Cox, 1995; Viola et al., 2006; De Paola et al., 2007; Wehrens et al., 2016). Hydrothermal ore deposits, where fault  
123 networks focus relatively large volumes of ore fluids and precipitate economic minerals (Cox et al. 2001; Boiron et al., 2003;  
124 Moritz et al., 2006; Scheffer et al., 2017a) are also pertinent examples of significant deformation-controlled fluid ingress.

125 The seismogenic depth down to 10-15 km (e.g. Kohlstedt et al., 1995) is thus a key region of the crust where to study the whole  
126 range of fluid-rock interaction processes occurring within fault zones. Deformation at that depth might be accommodated under  
127 overall brittle-ductile conditions along fault systems crossing or rooting into the brittle ductile transition zone (BDTZ). In detail,  
128 the deformation style in the BDTZ is generally characterized by the cyclicity, also at the short time scale, between brittle and

Formattato: Colore carattere: Rosso

Formattato: Colore carattere: Rosso

Formattato: Colore carattere: Rosso

Formattato: Colore carattere: Rosso

129 ductile behaviour (Famin et al., 2004; Famin et al., 2005; Siebenaller et al., 2013). This is induced and regulated by the complex  
130 and transient interplay of numerous parameters, among which the lithological composition and transient variation of temperature,  
131 pore pressure and strain rate within the deforming system. Field studies have documented unequivocally that ductile and brittle  
132 deformation may even be simultaneously active during deformation as a function of the transient and spatially heterogeneous  
133 evolution of the chemical and physical parameters steering deformation, leading to the broad coexistence of geological features  
134 expressing frictional deformation and viscous creep mechanisms and to mutual crosscutting relationships thereof (e.g., Guermani  
135 and Pennacchioni, 1998; Kjöll et al., 2015; Pennacchioni et al., 2006; Wehrens et al., 2016; Scheffer et al., 2017b).  
136 Veins are particularly important in this context because they attest to the relative abundance of aqueous fluids in the deformation  
137 history (e.g. Cox et al., 2001). Portions of the seismogenic crust that experience large fluid fluxes host pervasive large and  
138 vertically extensive vein networks (Sibson et al., 1988), within which up to several millions of m<sup>3</sup> of hydrothermal minerals may  
139 deposit from the flowing fluid (e.g. Heinrich et al., 2000; Cox, 2005; Bons, 2001; Garofalo et al., 2002). In contrast, portions of  
140 the crust deforming in the absence of significant fluid flow would show scarce evidence of- or no veining, with only synkinematic  
141 H<sub>2</sub>O-rich minerals within the fault rock attesting to hydrous conditions (cf. Mancktelow and Pennacchioni, 2004; Menegon et al.,  
142 2017).

143 The physical-chemical conditions of fluid-rock interaction in the BDTZ have been extensively studied within exhumed faults by  
144 applying a set of geochemical tools that include fluid inclusion data analysis (e.g. Morrison, 1994; Morrison and Anderson, 1998;  
145 Mulch et al., 2004; Ault and Selverstone, 2008; Garofalo et al., 2014; Siebenaller et al., 2016; Compton et al., 2017), determination  
146 of the isotopic compositions of fault fluids, and mass transfer calculations between host rock and fault rocks (e.g. Goddard and  
147 Evans, 1995; Garofalo, 2004; Mittempergher et al., 2014; Spruzeniece and Piazzolo, 2015). These data is approach yields important  
148 constraints on the PT conditions of fluid-rock interaction within the studied faults BDTZ, on the source region of the fluids  
149 reaching and flowing within the BDTZ deformation zones, and on element mobility during syn-tectonic fluid flow. These studies,  
150 however, provide only limited information and do not specifically address the role of fluids on the potentially complex mechanisms  
151 that trigger and permit the aforementioned cycles of brittle-ductile deformation. Open questions thus remain, such as, for example,  
152 which pPressure, -tTemperature, -cComposition (P, T, X) conditions are best for a fluid to trigger brittle-ductile deformation  
153 cycles in a fault system within the BDTZ; and which fluid property is specifically most effective in controlling the cycles.

154 In this work, we follow a multidisciplinary approach by combining the meso- and microstructural observations with the  
155 geochemical analysis of fluids, petrographic documentation of fault rocks and veins, microthermometric properties of fluid  
156 inclusion assemblages, electron probe microanalyses (EPMA) of fault minerals, Raman spectrometry of fluid inclusions, and  
157 electron probe cathodoluminescence imaging to study the effects of numerous cycles of fluid-rock interaction that have occurred  
158 in a vein-rich deformation zone from within the seismogenic BDTZ of the seismogenic region of and now exhumed as part of  
159 the Paleoproterozoic continental crust of southwestern Finland. The studied deformation zone belongs to an exhumed conjugate  
160 fault system that experienced a complex history of structural reactivation and fluid flow. Deformation zone BFZ300, the target

Formattato: Colore carattere: Rosso

Formattato: Colore carattere: Rosso

Formattato: Colore carattere: Rosso

Formattato: Colore carattere: Rosso

Formattato: Colore carattere: Rosso

Formattato: Colore carattere: Rosso

Formattato: Colore carattere: Rosso, Non Evidenziato

Formattato: Colore carattere: Rosso, Non Evidenziato

Formattato: Colore carattere: Rosso, Non Evidenziato

Formattato: Colore carattere: Rosso, Non Evidenziato

161 of our study, crops out at c. 426 m below sea level within the deep [Onkalo](#) nuclear waste repository that is presently being built  
162 in the island of Olkiluoto (Fig. 1a).

163 ~~We~~Our results allow us to constrain and [describe the progressive evolution of the deformation processes and the role of fluids](#)  
164 ~~activity~~ during ~~involved~~ both at [fault initiation and during the subsequent reactivation phases](#). We propose that [fluid pressure](#)  
165 ~~activity fluctuation cycles~~ combined with a general [within an overall ductile environment](#) at the BDTZ where deformation  
166 occurred by crystal plastic processes ~~triggered~~ the here proposed [brittle-ductile cyclicity](#) encompassing fracturing, vein  
167 precipitation and [crystal](#)-plastic deformation before renewed and fluid-induced embrittlement. Our multitechnique approach made  
168 it possible to determine many of the actual chemical and physical properties of the fluids involved in the deformation process,  
169 leading to a well-constrained conceptual mechanical model for the fault nucleation and subsequent development. ~~Quartz~~  
170 precipitation in opened fractures plus crystal plastic processes and viscous recovery helped the system to regain strength and  
171 pressurize, triggering a new hydrofracturing event. ~~The adopted integrated approach provides detailed and new insights into the~~  
172 [mechanisms steering deformation within the BDTZ](#). We propose a mechanical conceptual model that accounts for the constraints  
173 derived from our multidisciplinary approach.

## 174 2 Geological setting

175 The study area is located in southwestern Finland, on the island of Olkiluoto (Fig. 1a) within the Paleoproterozoic Svecofennian  
176 orogenic province, which is ~~characterized~~ [formed](#) by supracrustal high-grade metamorphic sequences and plutonic rocks. The  
177 most abundant lithologies in the study area are variably migmatitic metasedimentary rocks interleaved with up to [several](#) meter  
178 thick levels of metavolcanic rocks, [in addition to](#) calc-alkaline synorogenic TTG-type granitoids, ~~and as well as~~ late orogenic  
179 leucogranites (Figs. 1a, 1b). For a detailed lithological characterization of the area, we refer the reader to Hudson and Cosgrove  
180 (2006) and Aaltonen et al. (2016).

181 Numerous studies carried out on Olkiluoto have highlighted the long geological evolution of the region, which is commonly  
182 summarised by tectonic models ~~for the Paleoproterozoic evolution of southern Finland~~ proposing either an evolution during a  
183 single and semi-continuous Svecofennian orogenic event (Gorbatshev and Bogdanova, 1993) or, ~~instead~~ [alternatively](#), a sequence  
184 of up to five distinct accretion events leading to the amalgamation of several microcontinents and island arcs at the margin of the  
185 Archean craton between 1.92 and 1.79 Ga (e.g. Lahtinen et al., 2005). In this scenario, several subduction systems developed,  
186 and the collision of the involved microcontinents and island arc complexes resulted in conspicuous continental growth, forming  
187 the major part of the Paleoproterozoic domain of the Fennoscandian Shield (1.89-1.87 Ga). According to Lahtinen et al. (2005),  
188 this “Fennian accretionary event” ended with a phase of orogenic collapse associated with regional extension and remarkable  
189 crustal thinning between c. 1.86 and 1.84 Ga. Renewed compression ensued during collision of the “Sarmatian Plate” with the  
190 previously consolidated Svecofennian Shield, causing major crustal shortening, high temperature regional metamorphism  
191 (Kukkonen and Lauri, 2009) and the emplacement of S-type granites (e.g. Ehlers et al., 1993). Tectonic activity ascribable to this  
192 orogenic phase ceased with a [new distinct](#) orogenic collapse [phase](#) at 1.79-1.77 Ga (Lahtinen et al., 2005).

193 Pervasive reworking of the Svecofennian domain took place in the Mesoproterozoic when the crust underwent significant  
194 stretching and was intruded by voluminous Rapakivi granites and diabase dykes resulting from the widespread melting of the  
195 lower crust at c. 1.65-1.50 Ga. This tectonic phase was probably due to the development of a rift along the present Baltic Sea  
196 (Korja et al., 2001). Crustal thinning caused also the formation of the “Satakunta Graben”, a NW-SE trending graben located c.  
197 50 km to the north of Olkiluoto, which was later filled by Mesoproterozoic sandstone (Jotnian sandstones, Fig. 1a). The latest  
198 stage of crustal evolution in southern Finland is expressed by the intrusion of 1.27-1.25 Ga, N-S striking -olivine diabase dikes  
199 (Fig. 1a; e.g., Suominen, 1991).

200 As to the structural evolution of the study area, the bedrock was affected by complex, polyphase ductile deformation between  
201 1.86 and 1.81 Ga. According to the evolutionary deformation scheme ~~proposed~~ by Aaltonen et al. (2010) the results of up to five  
202 different phases, referred to as D<sub>1</sub>-D<sub>5</sub>, are preserved in the local structural record, each characterised by structures with distinctive  
203 mineral composition, metamorphic grade, geometry and kinematics. The most relevant phases to our study are D<sub>2</sub> to D<sub>4</sub>. During  
204 these ductile episodes, a regional and pervasive NE-SW striking and moderately SE-dipping foliation developed, strain localized  
205 along mesoscopic shear zones parallel to subparallel to the foliation and extensive migmatization occurred under amphibolite-  
206 facies metamorphic conditions. NNE-SSW and N-S striking mylonitic shear zones also formed under those conditions, whereas  
207 later ductile events developed under progressively lower-grade metamorphism until c. 1.7 Ga ago, when brittle deformation  
208 became the dominant deformation style in response to progressive regional exhumation and cooling (Mattila and Viola, 2014;  
209 Aaltonen et al., 2016). The penetrative, inherited ductile grain that by then characterised the crystalline basement and that was  
210 suitably oriented with regard to the prevailing stress field was invariably reactivated. This is the case for several NNE-SSW  
211 striking faults mapped underground in the Onkalo repository, which clearly overprint earlier D<sub>4</sub> shear zones and fully exploit the  
212 pre-existing ductile precursors. ~~Other faults, such as BFZ300, do not show any clear genetic relation to the older ductile  
213 fabric and cut it discordantly.~~

214 ~~As will be shown in the following section,~~ BFZ300 belongs to a set of subvertical, conjugate brittle-ductile to fully brittle strike-  
215 slip faults characterized by N-S-trending sinistral and NW-SE dextral faults. Both sets ~~show document~~ a complex history of  
216 reactivation and contain evidence for cyclic and transient switches between brittle and ductile deformation at all scales. Meso-  
217 and microstructural studies show that the sinistral faults overprint and probably reactivate a dextral ~~viscous-mylonitic~~ precursor  
218 related to earlier, localized ductile deformation (Prando et al., in prep.). These faults locally contain pseudotachylyte injections,  
219 which ~~potentially suggests~~ seismic behaviour during deformation (Menegon et al., 2018). In contrast, dextral faults cut across the  
220 foliation, do not exploit any ductile precursors and do not host pseudotachylytes. ~~The fault zone studied here~~BFZ300 belongs to  
221 this second group of faults. In the following, we describe its architecture, reconstruct its deformation history and constrain the  
222 deformation mechanisms and faulting conditions that ~~acted-prevalled~~ during its nucleation and subsequent development. The  
223 architecture and deformation history of the remarkably different conjugate structure ~~of to~~ BFZ300, which is a sinistral  
224 brittle-ductile deformation zone, ~~whose seismic brittle failure was steered by the presence of a penetrative ductile  
225 precursor, will be~~ described in ~~a the separate~~ Part II companion paper (Prando et al., in prep.).

### 3 Applied methods: Fluid inclusion, mineral chemistry and EBSD analyses

Field documentation and sampling were carried out at the underground BFZ300 exposures of Onkalo, which are necessarily limited in extent but that, together with the logged diamond drill holes from the underground exploration, allow a well-constrained 3D reconstruction of the local geology. The studied fault section is located at a depth of 426 m b.s.l. (Fig. 1b) and is about 8 m long. To characterize the fault architecture and constrain the spatial and temporal association of fault rocks and the type of fluid involved in the deformation, several outcrop samples, each representative of a distinct structural domain, were collected at the outcrop (TPH 2, TPH 3, TPH 4, TPH 5 and TPH 6), in addition to samples PH 21 and PH 22 from a diamond 154 drill core that intersects BFZ300 at the same depth in an area that is currently not excavated (Fig. 3). From these samples we prepared 10 petrographic thin sections (samples: TPH120-2, TPH 120-4, TPH 120-6, PH 21 and PH 22) and 9 doubly-polished sections for fluid inclusion analysis (thickness: ~150 µm, samples: TPH120-2, TPH 120-4, TPH 120-6, PH 21 and PH 22). Due to the extensive reactivation of the fault zone and the consequent obliteration of the FI record, FI study was carried out only in samples TPH 120-4, TPH 120-6, PH 21. Hand samples and drill cores localities are specified in Fig. 2.

Microstructural work was carried out on oriented petrographic thin sections cut orthogonally to the foliation and parallel to the striae that track the overall strike-slip kinematics of the deformation zone. Striae are defined by elongated trails of chlorite grains, at the vein-host rock boundary.

Field documentation and sampling were carried out at the underground Onkalo BFZ300 exposures of BFZ300 (Fig. 1b) Onkalo which ~~are~~ were necessarily limited in extent to the actual excavated volume of rocks at the time of our study but that, together with the logged diamond drill holes-cores from the underground exploration, allow a well-constrained 3D reconstruction of the local geology.

#### 3.1 Fluid inclusions and mineral chemistry

Fluid inclusion measurements were conducted on “fluid inclusion assemblages” – FIAs, i.e. on petrographically discriminated, cogenetic groups of fluid inclusions located along trails or (less commonly) within clusters (Bodnar, 2003a; Goldstein, 2003). By definition, FIAs are groups of inclusions that have been trapped together (i.e., they are cogenetic) at a specific stage of mineral formation (i.e. co-genetic); and, as such, give the highest level of confidence when characterizing the properties of trapped fluids and discriminating possible stages of post-entrapment re-equilibration (Bodnar, 2003b, and references, therein). We identified appropriate FIAs that constrain the deformation history of BFZ300, but also applied the Roedder’s identification criteria of FIAs according to the timing of entrapment (i.e., primary, secondary, pseudosecondary) in order to link stages of fluid entrapment with stages of brittle and ductile deformation of quartz. In this regard, we considered as co-genetic, and therefore representative of a one specific stage of brittle deformation and fluid circulation, only those FIAs that exhibited both similar orientation and petrographic characteristics at the scale of the thin section. can consider FI trails as synkinematic features, where FIAs are entrapped during stages of brittle deformation and fluid circulation, such that FIAs arranged along trails of the same orientation and with similar petrographic features might be representative of the same deformational event.



259 In the selected samples, we studied ~~2842~~ FIAs entrapped within two distinct generations of quartz (~~named Qtz I and Qtz II~~)  
260 ~~infilling-forming~~ two different generations of veins (~~named Qtz I and Qtz II~~) and exhibiting the least petrographic evidence of  
261 post-entrapment overprinting by later ductile and/or brittle deformation, which provided c. ~~800400~~ microthermometric properties.  
262 Due to the well-documented tendency of fluid inclusions to modify their shape, volume, and composition after their initial  
263 entrapment even at low deviatoric stress conditions (e.g. Diamond et al., 2010; Kerrich, 1976; Tarantola et al., 2010; Wilkins and  
264 Barkas, 1978), working on FIAs that ~~show the are similar as possible to those preserving the pristine fluid conditions is essential~~  
265 ~~when aiming at the study of the original physical and chemical properties of the fluid involved in the fault activity. lowest least~~  
266 ~~possible degree of textural re-equilibration~~ is essential when aiming at ~~the study~~ constraining of the original physical and chemical  
267 properties of the fluid(s) involved in the fault activity.

268 Microthermometric properties of fluid inclusions were determined at the Department of Biological, Geological and  
269 Environmental Sciences of the University of Bologna using a Linkam THMSG 600 heating/freezing stage coupled with an  
270 Olympus BX51 polarizing microscope. The microthermometry stage was calibrated by using synthetic fluid inclusion samples at  
271 -56.6, 0.0, and 374 °C, which correspond to the melting of CO<sub>2</sub>, ice melting, and final homogenization of H<sub>2</sub>O inclusions,  
272 respectively. Obtained accuracies were ±0.3 °C for final ice melting temperature (T<sub>mice</sub>) and ±3 °C for final homogenization  
273 temperature (T<sub>hot</sub>). In order to produce an internally consistent dataset, all phase transitions were exclusively collected for  
274 individual FIAs and measured ~~by-with~~ the same standard procedure. Samples were first rapidly cooled to c. -180 °C and then  
275 slowly heated to detect the potential formation of a solid carbonic phase, eutectic phases, salt hydrates, ice, and clathrates. The  
276 T<sub>hot</sub> were later determined in the FIAs by heating the samples from room temperature and recording the mode of homogenization  
277 (i.e., by bubble or liquid disappearance). All phase transitions were measured by using the cycling method described by Goldstein  
278 and Reynolds, (1994), and care was taken also ~~into~~ recording the minimum and maximum values for each assemblage. Volume  
279 fractions of individual fluid inclusions determined as % of the ratio  $\phi = V_v/V_{tot}$  (cf. Diamond, 2003), were estimated optically at  
280 room temperature using calibrated charts. Salinity, bulk densities and isochores were computed from the measured T<sub>mice</sub> values  
281 using the HokieFlincs Excel spreadsheet (Steele-MacInnis et al., 2012 and reference therein).

282 ~~Fluid inclusions were also analysed using m~~Micro-Raman ~~spectrometric analysis of fluid inclusions was spectrometry. Analyseis~~  
283 ~~were~~ carried out at the Department of Mathematical, Physical and Computer Sciences of the University of Parma (Italy) using a  
284 Jobin-Yvon Horiba LabRam spectrometer equipped with He-Ne laser (emission line 632.8 nm) and motorized XY stage. The  
285 spectral resolution of the measurements was determined as nearly 2 cm<sup>-1</sup>. The confocal hole was adjusted to obtain a spatial  
286 (lateral and depth) resolution of 1–2 μm. Most spectra were obtained with a 50× objective (N.A. 0.75), although for shallow  
287 inclusions also a 100× objective (N.A. 0.90) was used. The calibration was made using the 520.7 cm<sup>-1</sup> Raman line of silicon. A  
288 wide spectral range (100–3600 cm<sup>-1</sup>) was scanned for each inclusion for the presence of CO<sub>2</sub>, N<sub>2</sub>, CH<sub>4</sub>, and H<sub>2</sub>S, but the final  
289 acquisitions were made mainly between 1100 and 1800 cm<sup>-1</sup> for the study of CO<sub>2</sub> spectra, and between 2500 and 3300 cm<sup>-1</sup> for  
290 CH<sub>4</sub> and H<sub>2</sub>S. The acquisition time for each spectral window was 120–240 s, with two accumulations. The power on the sample

291 surface is nearly 1 mW but the power on the analysed inclusions has to be considered lower due to reflections and scattering.  
292 Analyses were carried out on the vapour bubbles of the fluid inclusions.  
293 After the calculation of representative fluid inclusion isochores for each FIA, the pressure corrections were assessed by using the  
294 crystallization temperatures of two mineral pairs – namely chlorite-quartz and stannite-sphalerite – as independent input  
295 parameters ~~for Qtz I and Qtz II veins, respectively~~. Chlorite-quartz temperatures were calculated by using the method of Bourdelle  
296 and Cathelineau (2015), which assumes quartz-chlorite equilibrium and uses ratios of chlorite end-member activities to link the  
297 chlorite compositions with the corresponding formation temperatures through the quartz-chlorite equilibrium constants. This  
298 method is based on the measurements of the concentrations of the major chlorite components (Si, Fe, Mg) and can only be applied  
299 to chlorites with  $(K_2O + Na_2O + CaO) < 1wt\%$ , indeed the case of our chlorites. To estimate the formation temperature of  
300 cogenetic sulphides associated with Qtz II we used the stannite-sphalerite formation temperature following the method proposed  
301 by Shimizu and Shikazono (1985). This geothermometer uses the temperature dependency of iron and zinc partitioning between  
302 stannite and sphalerite (Nekrasov et al., 1979) as a ~~useful~~ temperature indicator of the association Qtz II-stannite and sphalerite.

### 303 **3.2 Electron Probe Microanalysis Microanalysis**

304 Electron Probe Microanalysis (EPMA) of fault minerals ~~were was~~ carried out ~~by using with~~ a JEOL-8200 wavelength-dispersive  
305 electron microprobe housed at the Department of Earth Sciences of the University of Milan, Italy. The instrument fits 5 WDS  
306 spectrometers utilizing lithium fluoride (LiF), pentaerythritol (PETJ and PETH), and thallium acid phthalate (TAP) analysing  
307 crystals and an optical microscope. Samples were probed with a beam size of  $\sim 1 \mu m$  at 15 keV and 5 nA beam current. Synthetic  
308 and natural materials were used as calibration standards at the beginning of each session. Analytical 1- $\sigma$  errors are typically  $< 4\%$   
309 for major elements and for the minor elements.

310 Panchromatic cathodoluminescence (CL) imaging was ~~also~~ performed by using the CL CCD detector adjacent to the optical  
311 microscope of the JEOL-8200 on the sections used for microstructural work. The electron beam was focused on the sections with  
312 an accelerating voltage of 15 kV and 30 nA beam current. Black/white digital images were collected with a 40x magnification by  
313 beam mapping with the CCD detector at a spatial resolution of  $1 \mu m$  (beam resolution), which resulted in imaged areas of  $27.8 \times$   
314  $22.2$  mm. The exposure time for image acquisition was 120 s.

315 Petrographic thin sections were later also analysed ~~used at the Scanning Electron Microprobe (SEM) to investigate the~~  
316 crystallographic preferred orientation (CPO) of the selected sites of the quartz veins from the fault core (sample name TPH-  
317 120-4, see Figure 2 for sample location). Sample Samples were as analysed using with a JEOL 6610 SEM equipped with a  
318 Nordlysif UF 1000 Nano EBSD detector, hosted at the Electron Microscopy Centre-School of Geography, Earth and  
319 Environmental Sciences of the University of Plymouth, UK. EBSD analysis details and the acquired images-detailed results  
320 are reported in the Supplementary Materials.

321

## 322 4 Results

### 323 4.1 BFZ300 fault architecture

324 ~~The studied fault BFZ300 section is located at a depth of 426 m b.s.l. and is about 8 m long (Fig. 2a).~~ It strikes NNW-  
325 SSE and dips very steeply to subvertically to the southwest (Fig. 2b). It cuts through high-grade veined migmatite, interlayered  
326 with gneiss and pegmatitic granite. ~~At the studied underground outcrop with a length of 8 m,~~ the fault is a strike-slip fault system  
327 formed by two main subparallel fault segments connected by a mesoscopic *sinistral* step-over zone. Subhorizontal striae *defined*  
328 *by elongated trails of chlorite grains* and kinematic indicators such as chlorite slickensides (Fig. 2c) and R and R' planes *invariably*  
329 indicate *invariably* dextral *strike-slip* kinematics. The most striking mesoscopic characteristic of BFZ300 is the presence in the  
330 fault core of a composite set of almost continuous quartz veins (between 1 and 20 cm in thickness) along the entire exposed strike  
331 length. A schematic representation of the fault zone is shown in Figure 32.

332 The fault contains a 0.5-2 m thick damage zone separated ~~by from~~ the *undeformed* host rock by two discrete bounding surfaces  
333 ( $Y_1$  planes according to Tchalenko, 1970 Fig. 2a). The damage zone can be defined in the field on the basis of the presence of a  
334 fractured volume containing sets of conjugate dextral and sinistral hybrid fractures (Fig. 3a) intersecting to form a tight acute  
335 angle of c. 38° (Figs. 2b, 3a). Laterally continuous, NNW-SSE striking *quartz-filled* Mode I fractures (joints) *invariably* bisect  
336 this angle (Figs. 2b, 3a), helping to constrain the stress field orientation at the time of fracture formation, with the greatest  
337 compressive stress axis  $\sigma_1$  parallel to the Mode I fracture strike and oriented c. NNW-SSE. Joints are sharp and have a regular  
338 spacing of c. 10 cm. ~~Quartz-filled~~ The joints and the hybrid fractures of the damage zone ~~forms contain quartz, referred to as Qtz~~  
339 ~~I hereinafter, forming~~ veins up to 1-1.5 cm ~~in thickness~~ *thick and is referred to as Qtz I hereinafter* (Fig. 3a). Fractures and faults  
340 decorated by Qtz I have a translucent look that reflect the generally fine grain size of Qtz I (< 1 cm, Fig. 3b). Locally they are  
341 formed by en-echelon tensional segments connected by shear planes not decorated by any quartz infill (Fig. 3b). Joints occur also  
342 as barren fractures defining a penetrative sympathetic fracture cleavage (*sensu* Basson and Viola, 2004; *green lines in Fig. 2b*).  
343 *Field evidence also suggests that* fracture density within the damage zone tends to increase towards the fault core.

344 The fault core is bounded by two main discrete slip surfaces ( $Y_1$ , Figs. 2a, and 3d, f, h). It contains, and is defined by, two distinct  
345 generations of quartz veins (Fig. 3c) that are interrupted and offset laterally by a metric *sinistral* step-over zone (Fig. 3d-f). The  
346 main quartz vein of the core is infilled by quartz exhibiting the same mesoscopic appearance of Qtz I in the damage zone; we  
347 therefore refer to it as a Qtz I vein. It is accompanied by a younger, subparallel vein formed by a milky-white type of quartz with  
348 a significantly larger *quartz* grain size than Qtz I (>1 cm) that we refer to as Qtz II (Fig. 3c). Locally, pockets of cataclasis and  
349 breccia *formed at the expense of the host migmatitic gneiss* are also observed along and in between the two veins (Figs. 3g, i).  
350 ~~These shears are formed by cataclastic bands formed at the expense of the host migmatitic gneiss.~~ The Qtz II vein ~~shows exhibits~~  
351 a quite irregular, curved geometry (Figs. 3c, h) and a variable thickness up to a maximum of c. 20 cm. The minimum Qtz II vein  
352 thickness coincides spatially with an ~~an~~ *lateral* apparent *lateral* displacement of the vein. The BFZ300 core varies in thickness  
353 between 20 and 30 cm along most of the exposed fault length, but becomes thicker (up to 50 cm) in the compressional step-over

354 zone that connects the two fault segments that are offset laterally by c. 1 m. The sinistral step-over zone is defined by synthetic T  
355 fractures (Figs. 3d,e) and contains a decimetric brecciated lens (Fig. 3d). T fractures are generally filled by Qtz I veins (Fig. 3e).  
356 Chlorite is present as a secondary phase, with a modal abundance between 5 and 10 vol% in both Qtz I and Qtz II veins. In Qtz I  
357 veins it occurs as euhedral/subhedral crystals ~~that are~~ up to 1-2 mm in size (Fig. 3g). Chlorite is present mostly as a disseminated,  
358 interstitial phase, concentrated mainly in the internal part of the Qtz I veins (Fig. 3g). In the Qtz II vein, however, it occurs as  
359 elongated crystals (5-8 mm in length) arranged perpendicularly to the walls of the vein, which suggests orthogonal dilation at the  
360 time of opening (Fig. 3h). The Qtz II vein contains also small (1-2 cm) aggregates of sulphides (sphalerite, pyrite, galena, and  
361 chalcopyrite) mainly concentrated in the central part of the vein (Fig. 3g).

362 As observed in the field, the presence of Qtz I veins along the joints in the damage zone and the continuity of the fault core Qtz I  
363 vein suggest Mode I fracturing during Qtz I emplacement (Figs. 2a, 3a,c, and 2a). The semi-continuous parallelism of Qtz I and  
364 Qtz II veins in the fault core, combined with the location of the Qtz II vein along the walls of the Qtz I vein, suggest the partial  
365 reactivation of the Qtz I vein during Qtz II emplacement. Dilation leading to Qtz II emplacement exploited and further reworked  
366 the Qtz I-host rock contact, that seemingly had a lower tensile strength than the pristine migmatite. The reconstructed time  
367 relationship between the two vein generations is also consistent with local evidence of the Qtz II vein partially-partly crosscutting  
368 ~~parts of~~ the Qtz I vein (Fig. 3f).

#### 369 4.2 BFZ300 microstructural analysis

370 To constrain the spatial and temporal association of fault rocks and the type of fluid involved in the deformation, several outcrop  
371 samples, each representative of a distinct-specific structural domain, were collected at the studied underground outcrop (TPH-  
372 120-2, TPH-120-3, TPH-120-4, TPH-120-5 and TPH-120-6), in addition to samples PH-21 and PH-22 from diamond drill cores  
373 that intersect BFZ300 at the same depth in an area that is currently not excavated. From these samples we prepared 10 petrographic  
374 thin sections (samples: TPH-120-2, TPH-120-4, TPH-120-6, PH-21 and PH-22) and 9 doubly-polished sections for fluid  
375 inclusion analysis (thickness: ~150 µm, samples: TPH-120-2, TPH-120-4, TPH-120-6, PH-21 and PH-22). Due to the extensive  
376 reactivation of the fault zone and the consequent obliteration of the FI record, the FI study was carried out only in samples TPH-  
377 120-4, TPH-120-6 and PH-21. Hand samples and drill cores localities are specified shown in Figure 3.  
378 The microstructural work was carried out on oriented petrographic thin sections cut orthogonally to the migmatitic foliation  
379 and parallel to the striae/slides.  
380 In the following we provide a description of the microstructural characteristics of BFZ300 by detailing our findings and  
381 observations separately for the main structural domains of the fault zone.

##### 383 4.2.1 Damage zone

384 Qtz I veins within the damage zone cut across the migmatitic host rock and form the infill of conjugate sets of hybrid fractures,  
385 which, when studied at the microscale, appear as formed by dilatant segments joined by cataclastic shear fractures (Fig. 4a).

386 Shearing ~~on the latter~~ is well documented by the asymptotic bending into the shear surfaces of foliation planes formed by the  
387 alignment of chlorite and muscovite, both partly altered to sericite and chlorite, respectively (Fig. 4a). Qtz I infilling the tensional  
388 segments has an average grain size between 200  $\mu\text{m}$  and 3 mm and exhibits a rather heterogeneous texture, from purely blocky  
389 to mixed elongated-blocky (Figs. 4b,c). The largest crystals (800  $\mu\text{m}$  to 1 mm) are elongated and stretched from the vein walls  
390 towards the inner part of the vein (Figs. 4c, ~~and~~ 5a), ~~which is consistent with a syntaxial growth mechanism (Bons et al., 2012).~~  
391 At least two episodes of vein growth/renewed dilation, as indicated by the presence of median lines (ML), are ~~clearly~~ visible  
392 within one of the studied veins and confirm a syntaxial growth mechanism for the vein (Fig. 5; e.g. Bons et al., 2012). Medial  
393 lines are defined by the alignment of chlorite, sericite, and carbonate aggregates (Figs. 5a, b, d). Blocky euhedral quartz crystals  
394 are also found ~~varying in~~ with a grain size between 300 ~~and~~ 600  $\mu\text{m}$ . These crystals are juxtaposed ~~against~~ to very fine grained  
395 quartz (<200  $\mu\text{m}$ ) within sericite-rich cataclastic bands (Fig. 4b). These cataclases contain also hydrothermally altered host-  
396 rock fragments including pervasively altered K-feldspar-bearing lithic fragments and phyllosilicates.

397 With the exception of the blocky variety, Qtz I crystals exhibit various degrees of crystal-plastic deformation and recovery. They  
398 contain widespread evidence of undulose extinction and extinction bands (Fig. 5b), and incipient bulging along grain boundaries  
399 is also evident (Fig. 5c) ~~indicating distributed internal plastic deformation. Millimetric intracrystalline barren fractures are also~~  
400 recognized in the samples (e.g. Fig. 5c). Cathodoluminescence imaging of Qtz I from the damage zone also confirm shows the  
401 presence of a diffuse dense network of healed quartz microfractures (Fig. 4d), which demonstrates healing subsequent to brittle  
402 deformation and fracturing.

403 Chlorite ~~occurs as a disseminated phase~~ occurs along the median lines ML of the veins, secondary cracks, at along grain boundaries  
404 and as inclusions within quartz crystals, within the Qtz I veins of the damage zone and in textural equilibrium with quartz It  
405 has a peculiar vermicular texture (Fig. 5db) and, crystal dimensions of about up to 50-100  $\mu\text{m}$ , and displays interference colours  
406 ranging from violet to Berlin blue. Vermicular chlorite forms small pockets mainly located in the central part of the veins and at  
407 the triple junctions of blocky quartz crystals.

#### 408 4.2.2 Fault core

409 In the BFZ300 fault core, the Qtz I grain size reaches the smallest observed value (range: 30-800  $\mu\text{m}$ , Fig. 6a) grain size, although  
410 it of Qtz I is strongly variable within the vein, suggesting the presence of heterogeneous and complex structural sub-domain s,  
411 of deformation. Qtz I has the smallest observed grain size (range: 30-800  $\mu\text{m}$ , Fig. 6a) and documents multiple and cyclic episodes  
412 of mutually overprinting brittle and ductile deformation leading to a complex microstructural record. The earliest post-vein  
413 emplacement recognised deformation stage is reflected by the low-temperature, intracrystalline deformation of the largest crystals  
414 (400-800  $\mu\text{m}$  in size). Typical microstructures, such as Undulose extinction, wide extinction bands (WEBs, Derez et al., 2015),  
415 and bulging along grain boundaries are the most common microstructures ascribable to this deformation stage (Figs. 6a, b, b).  
416 A distinct first brittle deformation event is documented by narrow, intracrystalline fractures that crosscut the largest quartz  
417 crystals (Figs. 6b, and c); and which locally contain new grains of quartz ranging in size between 20-100  $\mu\text{m}$  (Fig. 6d). More in

418 detail, these new grains form parallel bands that are oriented at low angle ( $<30^\circ$ ) to the vein walls and that can be up to 2 mm in  
419 length and 200  $\mu\text{m}$  in thickness. Plastically deformed Qtz I crystals hosting these intracrystalline bands of new grains are cut  
420 across by another distinct later set of subparallel intercrystalline fractures, which are interpreted as the expression of yet another  
421 deformation event that occurred under overall brittle conditions. These fractures are parallel to the strike of BFZ300 and are in  
422 turn sealed by partly recrystallized new quartz grains (grain size: 50-150  $\mu\text{m}$ ; Fig. 6c). Petrographic analysis on intercrystalline  
423 fractures also show that they are also locally decorated by trails of fluid inclusions (Fig. S2 Supplementary Materials) and that  
424 they can be up to 2.5 cm in length and up to 500  $\mu\text{m}$  in width (Fig. 6a). Their cathodoluminescence imaging of these fractures  
425 shows that they are sealed and healed, yielding an homogeneous dark cathodoluminescence signal (Figs. S1a-b of in the  
426 Supplementary Materials). They are locally decorated by trails of fluid inclusions (Figs. S2a, d of the Supplementary Material)  
427 and can be up to 2.5 cm in length and up to 500  $\mu\text{m}$  in width (Fig. 6a). EBSD maps were performed-acquired along some of these  
428 intercrystalline bands, and results suggest that the new grains sealing the fractures reflect the combined effect of initial cracking,  
429 grain nucleation and subsequent partial dynamic recrystallization filled by quartz new grains (EBSD maps and their location  
430 across the thin section are reported in Figs. S2b, c of the Supplementary Materials). The EBSD results highlighted indicate that  
431 recrystallization of Qtz I occurred prevalently by bulging and subgrain rotation recrystallization but also suggest that along the  
432 sealed intercrystalline fractures express the delicate interplay of both brittle and crystal plastic recrystallization processes are  
433 competing deformation. This is also in accordance with the petrographically contiguity of brittle fractures marked by fluid  
434 inclusions and recrystallized intercrystalline fractures.

435 Qtz II within the fault core is typically coarse grained (individual crystals: 300  $\mu\text{m}$ -1 cm in size) and exhibits a regular blocky  
436 texture devoid of any shape or crystal preferred orientation (Fig. 7a). Locally, these large crystals display primary growth textures,  
437 such as primary FIAs oriented parallel to specific crystallographic planes. With the exception of undulose extinction, Qtz II does  
438 not show clear evidence of plastic deformation, although cathodoluminescence imaging of optically continuous Qtz II has also  
439 shown that a dense network of healed quartz microfractures locally crosscuts Qtz II crystals (Fig. 7c). These are relatively thin  
440 (hundreds of  $\mu\text{m}$  thick) networks that are poorly visible to invisible by standard petrographic analysis. The only petrographic  
441 evidence for these healed microfractures within quartz are well defined trails of fluid inclusions crosscutting primary growth  
442 bands (Fig. 7d).

443 Chlorite is the second most abundant phase within the fault core Qtz I and Qtz II veins and occurs with a variety of textures.  
444 Aggregates of vermicular chlorite similar to that occurring in the damage zone (Fig. 5d) are also present in the Qtz I from the  
445 core (Fig. 8e), although chlorite with flaky and radiate textures (Fig. 8f) is also present. The latter type is generally 100-300  $\mu\text{m}$   
446 in size and is in textural equilibrium with quartz and rare calcite. Radiate chlorite overgrowing fractured Qtz II (Figs. 7b-e)  
447 suggests late Qtz II precipitation.

448 Associated with Qtz II, a sulphide assemblage made of pyrite, sphalerite, galena, and chalcopyrite (Figs. 7d, and e, see also Fig.  
449 , see also Fig. 3gb) forms aggregates that are commonly located along quartz grain boundaries. In the studied sections, these

450 aggregates have dimensions between 10 and 600  $\mu\text{m}$ . ~~Chalcopyrite occurs as  $\mu\text{m}$ -sized, irregular inclusions within sphalerite~~  
451 ~~forming the typical “chalcopyrite disease” texture (e.g., Barton and Bethke, 1987; Fig. 7e).~~  
452 Multiply reworked breccias and cataclases ~~occur within and~~ crosscut BFZ300. In the studied sections, a cataclastic band between  
453 5 and 8 mm thick crosscuts both Qtz I and Qtz II veins (Fig. 8a), but is in turn crosscut by a different quartz-radiate chlorite vein  
454 displaying evidence of syntaxial growth. This cataclase contains poorly sorted and angular quartz clasts ~~varying in size~~ between  
455 8 and 12 mm ~~in size~~ set in a finer (20-200  $\mu\text{m}$  in size) white mica-quartz matrix. The largest quartz fragments show irregular,  
456 lobate grain boundaries and are affected by undulose extinction. We interpret these textures as the product of dissolution and  
457 cataclastic reworking of ~~Qtz I-vein, a previous generation, plastically deformed quartz.~~  
458 Parallel sets of stylolitic seams ~~strike-trend c.~~ N-S<sub>2</sub> parallel to the strike of BFZ300<sub>2</sub> and mark the two sides of the cataclastic band  
459 (Figs. 8a, c). They host anhedral sphalerite, stannite, galena, pyrite, and chalcopyrite (Fig. 8d), which are coeval with the formation  
460 of ~~the~~ Qtz II vein. We interpret the presence of these anhedral sulphide minerals along the stylolite as the product of passive  
461 concentration by ~~pression-solution~~ processes. ~~We use the stannite-sphalerite mineral pair as a geothermometer for the Qtz II~~  
462 ~~emplacement (see below).~~

463

#### 464 4.3. Fluid inclusion data

##### 465 4.3.1 Fluid inclusion petrography

466 The studied FIAs contain invariably a two-phase fluid (liquid-vapour) and are mainly arranged in secondary trails within Qtz I  
467 crystals in the damage zone (Type S1) and also within Qtz I fault core, where they form dismembered (Type S2) trails and also  
468 appear as individual clusters inside the crystals affected by ~~intra-crystalline viscous-crystal-plastic~~ deformation (Type S3). Within  
469 ~~the~~ Qtz II ~~fault core~~, FIAs are arranged as pseudosecondary (Type PS) and secondary (Type S4) trails. Representative examples  
470 of FI petrographic features are shown for each BFZ300-structural domain in Fig. 9. Table 1 ~~gives-provides~~ a schematic  
471 representation of the location of the FI types ~~presented above~~, in addition to their location ~~within~~ the fault architecture and their  
472 fluid properties.

473 *Damage Zone:* Within Qtz I grains (Figs. 9a, ~~and~~ b), secondary FIAs are found as trails (Fig. 9a) that parallel what we interpret  
474 as healed, old ~~intra-crystalline~~ microfractures. ~~These microfractures are likely to be old joints and hybrid fractures whose~~  
475 ~~orientation mimics that of the mesosopic BFZ300 structural features.~~ In these assemblages, FIAs have a maximum size ~~ranging~~  
476 between 2 and 20  $\mu\text{m}$ , a regular equidimensional shape (i.e. negative crystal morphology), and ~~a relatively uniform volume~~  
477 ~~fraction,  $\phi$  ( $\phi = V_f/V_{tot}$ , see section 3) ranging between (volume fractions)  $\phi$  of 5 and -15%~~ (Fig. 9b).

478 *Fault Core:* Qtz I grains host secondary FIAs (Type S2), which are transgranular trails (Fig. 9c) ~~representing along~~ healed joints  
479 and hybrid fractures. These trails are locally interrupted and dismembered by aggregates of new, fine-grained quartz grains (Fig.  
480 9c), and generate a texture that is indeed typical of Qtz I from the fault core (~~cf-~~ Fig. 6a). Fluid inclusions ~~entrapped along these~~  
481 ~~trails (Type S2)~~ vary in size between 1 and 10  $\mu\text{m}$ , have a  $\phi$  of 10-20%, and show a negative crystal morphology (Fig. 9d). Fluid  
482 inclusions are also found as isolated clusters inside intensely recrystallised quartz domains (Fig. 9c). FIAs inside these

483 recrystallized quartz domains were pervasively obliterated during later episodes of ductile deformation. The development of  
484 WEBS, intercrystalline bands and bulging (cf. Fig. 6) resulted in the ~~transposition remobilization (i.e., “transposition” sensu~~  
485 ~~Anderson et al., 1990)~~ of these assemblages. ~~This is invariably regularly~~ observed and is documented, for instance, by the presence  
486 of short, secondary trails of regularly shaped inclusion oriented at a high angle with respect to a longer, parent trail (Fig. 9c).  
487 Morphologically, these trails resemble the transposed trails documented in high-grade metamorphic rocks (Andersen et al., 1990;  
488 Van den Kerkhof et al., 2014). Different types of fluid inclusion morphologies are found within the intensely recrystallized quartz  
489 domains (Fig. 9f). Negative crystal morphology is observed in some areas of the selected samples, but it is uncommon. More  
490 typical is instead the “dismembered” morphology (cf. Vityk and Bodnar, 1995; Tarantola et al., 2010), which is observed in the  
491 relatively large inclusions (> 20 µm). This morphology is made of a central (often empty) inclusion, showing several tails and re-  
492 entrants, surrounded by a three-dimensional clusters of small “satellite” inclusions. These clusters might be arranged with a quasi-  
493 planar geometry inside the host (i.e. in a trail-like fashion). Another typical texture found in most assemblages is the “scaloped”  
494 morphology of small- to medium-sized inclusions (<10-15 µm), which is defined by the presence of indentations, embayments,  
495 irregularities, and sharp tips of the inclusion walls (Fig. 9f). Small inclusions (<1 µm) are also found at the edge of the straight,  
496 regular boundaries of new quartz grains; they are mostly dark, i.e. they are vapour-rich or empty, and are equant in shape (Fig.  
497 9e). Although small inclusions do not allow a microthermometric study of the fluid-phase behaviour in this structural domain, they  
498 confirm the complex reactivation history of BFZ300.

499 Qtz II contains both pseudosecondary (Type PS) and secondary (Type S4) assemblages (Figs. 9g, ~~ii, hj~~). The first type is arranged  
500 in trails, that cut at low angle the hosting quartz but not the neighbouring phases (e.g., chlorite,–). In these assemblages, FIs are  
501 relatively large (2-45 µm). ~~They and exhibit show~~ elongated shape and ~~their φ varies values~~ between 15 and 30 % (~~enlargement~~  
502 ~~in Fig. 9gh~~). Type S4 FIAs (Fig. 9hi) ~~have host~~ two-phase inclusions whose size (5-35 µm) is similar to that of PS trails, but  
503 show a φ between 30 and 40 % (Fig. 9ij).

504 ~~PRare~~ primary FIAs are also present along growth planes of Qtz II ~~and are best observed predominantly in the least deformed~~  
505 ~~Qtz II crystals~~, where they have a relatively large size (20-50 µm; ~~Figs. S3a, b, c of the Supplementary Material~~). ~~TElsewhere~~  
506 ~~they present irregular and “dismembered” textures, which suggest intense post-entrapment re-equilibration. Primary FI textures~~  
507 ~~are shown in Figure S3 of the Supplementary Materials.~~

508 In summary, our microtextural study shows that the FIAs to be selected for the microthermometric study are only those hosted  
509 within Qtz I and Qtz II crystals with ~~the minimum degree of little to no~~ recrystallization and whose inclusions have textures  
510 corresponding to the least intense post-entrapment re-equilibration (Bodnar, 2003b; and ~~references~~ therein; Tarantola et al.,  
511 2010). These are the pseudosecondary and secondary FIAs in which dendritic or transposed inclusions are absent, and in which  
512 the host quartz exhibits only undulose extinction (S1, S2, S4 and PS).

513

514 **4.3.2 Microthermometry**



515 *Damage Zone:* The majority of Secondary FIAs hosted within Qtz I from the damage zone (Type S1) show a range of  $T_{\text{mice}}$   
516 between -5.9 and -0.1 °C, which corresponds to a salinity of 0-9 wt% NaCleq (Fig. 10a). In these FIAs, final homogenization  
517 ( $T_{\text{hot}}$ ) occurs into the liquid phase (i.e. by disappearance of the vapour bubble) and mainly between 150-400 330 °C (Fig. 10e).  
518 *Fault Core:* The secondary FIAs hosted within Qtz I of in the fault core (Type S2) show a range of  $T_{\text{mice}}$  between -3.9 and 0 -8.2  
519 and -0.4 °C, which corresponds to salinities between 0 and 614 wt% NaCleq (Fig. 10b), and final homogenization occurs into the  
520 liquid phase by bubble disappearance is between 150-130 and 420-410 °C (Fig. 10f).  
521 *Pseudosecondary FIAs entrapped within Qtz II* The (Type PS) show a range of  $T_{\text{mice}}$  between -113.6 and 0-0.1 °C, which  
522 corresponds to a salinity range between 0 and -18 15-2 wt% NaCleq (Fig. 10c) and final homogenization occurs into the liquid  
523 phase and is comprised between 150 and 440 °C (Fig. 10g). *Secondary FIAs in Qtz II* The (Type S4) show a range of  $T_{\text{mice}}$  between  
524 -7.3-11 and 0 °C, which corresponds to a 0-15 10-9 wt% NaCleq range of salinity (Fig. 10d), while final homogenization into the  
525 liquid phase is comprised between 150-130 and 430 °C (Fig. 10h).  
526 As no gases were detected-determined during microthermometric analysis (i.e. melting of carbonic phase or clathrate hydrates  
527 were not detected during the freezing experiments), additional micro Raman analysis has been was performed on a set of  
528 representative FIAs (samples: TPH-120-4; TPH-120-6; PH21; PH22), on several FIAs for the detection of gases into the studied  
529 aqueous inclusions. Aqueous fluid inclusions hosted both by the Qtz I and Qtz II show peaks at the characteristic wavenumbers  
530 of  $\text{CH}_4$  (2917  $\text{cm}^{-1}$ ) and  $\text{CO}_2$  (1388  $\text{cm}^{-1}$ ). These peaks were determined as weak in all spectra, and  $\text{CO}_2$  detection was only  
531 sporadic in a few inclusions in of only one one of the sample of the fault core (TPH-120-4A). Such These spectroscopic  
532 determinations are consistent with the lack of microthermometric evidence for  $\text{CO}_2$  or  $\text{CH}_4$  occurrence in the FIAs, i.e., with the  
533 failure to detect melting of a carbonic phase or clathrate hydrates during the freezing experiments (cf. Rosso and Bodnar, 1995;  
534 Dubessy et al., 2001). Although spectroscopic detections, the  $\text{CO}_2$ - and  $\text{CH}_4$ -bearing inclusions are not systematically associated  
535 with distinct-specific quartz vein generations or-specific microstructures (i.e. intracrystalline healed cracks, WEB's planes,  
536 intercrystalline fractures). WTherefore, we can-not therefore associate the presence of  $\text{CO}_2$  and/or  $\text{CH}_4$  to any specific deformation  
537 stages of the fault.  
538 Such spectroscopic determinations are consistent with the lack of microthermometric evidence of carbonic phase or clathrate  
539 hydrates during the freezing experiments (cf. Rosso and Bodnar, 1995; Dubessy et al., 2001). The impossibility to detect  $\text{CO}_2$ -  
540 and  $\text{CH}_4$ -bearing fluids during the freezing experiments indicate a gas pressure that is systematically lower than that required to  
541 observe clathrate dissociation (e.g., 1.4 MPa in  $\text{CO}_2$ - $\text{H}_2\text{O}$  fluids, Rosso and Bodnar, 1995), i.e. it shows low gas concentrations.  
542 As a consequence, we have modelled the fluid phases as simple  $\text{H}_2\text{O}$ -NaCl systems.  
543 The impossibility to detect  $\text{CO}_2$ - and  $\text{CH}_4$ -bearing fluids via microthermometric determinations indicates a gas pressure in the  
544 analysed inclusions that is systematically lower than that required to observe clathrate dissociation (e.g., 1.4 MPa in  $\text{CO}_2$ - $\text{H}_2\text{O}$   
545 fluids, Rosso and Bodnar, 1995), i.e. it shows low gas concentrations. systemsOlkiluoto fluid. Considering the broad salinity  
546 range of 0.1-14 wt% NaCleq for the BFZ300 fluids (which corresponds to NaCl concentrations of 1.7 10-3 -2.4 M), we cannot  
547 estimate a maximum  $\text{CH}_4$  concentration.

Formattato: Pedice

Formattato: Pedice

Formattato: Pedice

Formattato: Pedice

Formattato: Pedice

Formattato: Pedice

Formattato: Pedice

Formattato: Pedice

Formattato: Pedice

Formattato: Pedice

Formattato: Pedice

Formattato: Pedice

#### 548 4.4 Chlorite and sulphide geothermometry

549 Chlorite composition has been determined for several generations of chlorites in association with Qtz I and II, namely vermicular  
550 chlorite associated with Qtz I from the damage zone, vermicular and radiate chlorite associated with Qtz I from the fault core,  
551 and radiate chlorite associated with Qtz II from the fault core (Table 2). Chlorite compositions are plotted in the classification  
552 diagram of Hey (1954) are shown in Figure 11a and they are expressed as function of the Fe/(Fe+Mg) -ratio (i.e. X<sub>Fe</sub>). Chlorite  
553 compositional data are presented for according to each the structural domain of the fault they are associated with and for the  
554 distinct chlorite to the corresponding textures. Vermicular chlorite associated with Qtz I in the damage zone has a X<sub>Fe</sub> range  
555 between 0.50 and 0.55, while vermicular chlorite associated with Qtz I from the fault core has a X<sub>Fe</sub> of 0.53. Radiate chlorite  
556 associated with Qtz I from the fault core has a X<sub>Fe</sub> range between 0.71 and 0.81 while radiate chlorite associated with Qtz II from  
557 the fault core is between 0.65 and 0.80, constraining. Then, dominant compositions are within the ripidolite and aphausiderite  
558 end-members. This plot highlights distinct clusters of chlorite compositions across the fault architecture as possible due to the  
559 distinct fault reactivation stages. The EPMA data show that, in general, the BFZ300 chlorites are Fe-rich (X<sub>Fe</sub> = Fe/(Fe+Mg)  
560 between c. 0.65 and 0.90), have concentrations of (Na<sub>2</sub>O+K<sub>2</sub>O+CaO) <1 wt%, and result mainly from a solid solution of the  
561 sudoite and daphnite end-members, i.e., of Mg<sub>2</sub>Al<sub>3</sub>(Si<sub>3</sub>Al)O<sub>10</sub>(OH)<sub>8</sub> – (Fe,Mg)<sub>5</sub>Al(Si,Al)<sub>4</sub>O<sub>10</sub>(OH)<sub>8</sub>. The dataset shows in  
562 particular that the compositions of the distinct chlorite generations vary systematically with vein generation, as shown by the  
563 vermicular chlorite associated with Qtz 417 I veins (Fig. 8e) with a X<sub>Fe</sub> between 0.65 and 0.67 and the radiate chlorite associated  
564 with Qtz I from the fault core and Qtz II (Figs. 8f and 7b) with a X<sub>Fe</sub> between 0.76 and 0.86.

565 Temperature-composition relationships for the quartz-chlorite pair portrayed in the T-R<sup>2+</sup>-Si diagram of Bourdelle and  
566 Cathelineau (2015) show that, in the hypothesis of quartz-chlorite equilibrium, the precipitation of vermicular chlorite within the  
567 Qtz I of the damage zone took place in the 175-245 °C range (green diamonds of Fig. 11a). This range is distinct from that of  
568 the vermicular and radiate chlorite from Qtz I of the fault core, which is probably c. >350 °C because the measured R<sup>2+</sup>-Si  
569 compositional parameters (R<sup>2+</sup> = Mg+Fe) plot at the edge of, or slightly outside, the calibrated region of the Bourdelle and  
570 Cathelineau plot (red diamonds of Fig. 11a). We stress that the high-T chlorite plots parallel to the 350 °C isotherm, suggesting  
571 that it precipitated most probably at the same, or at a similar, temperature. Radiate chlorite associated with Qtz II from the fault  
572 core is instead compatible with an equilibrium precipitation at 160-220 °C (light-blue diamonds in Fig. 11a).

573 The collected EPMA data show that the sulphides associated with Qtz II have compositions that approach those of pure phases  
574 (Table 3). Pyrite has trace element concentrations (Cu, As, Pb, Ni, Zn) that are in general below the EPMA detection limit, while  
575 galena, sphalerite, and chalcopyrite show only some significant trace contents of Fe and Zn (e.g., Fe: 0.22-1.00 wt% in galena;  
576 Zn: 0.11-3.95 wt% in chalcopyrite). Pyrite and sphalerite from the Qtz II veins (Fig. 7e) have trace element concentrations that  
577 are, again, mostly below detection limits.

578 The stylolites bordering the cataclastic bands described above and formed at the contact between the Qtz I and Qtz II vein contain  
579 pyrite, galena, and the sphalerite-stannite pair (Figs. 8a, c, d), with the latter showing the largest compositional variation. This  
580 pair represents a mineral geothermometer because the partitioning of Zn and Fe between sphalerite and stannite was demonstrated

581 to be temperature dependent but pressure independent (Nekrasov et al., 1979; Shimizu, ~~M~~ and Shikazono, 1985). In the fourteen  
582 analysed pairs, stannite shows a range of Zn concentrations varying between 0.48 wt% and 3.25 wt%, while those of Fe, Cu and  
583 Sn vary within narrow ranges (Fe: 12.74±0.56 wt%; Cu: 28.30 ±0.33 wt%; Sn: 27.65 ±0.71 wt%). Sphalerite in the pair has  
584 concentrations of Fe and Zn of 7.63±0.87 wt% and 56.68 ±1.17 wt%, respectively. These ranges allow the calculation of the  
585 partition coefficient ( $K_D$ ) of the reaction:  $\text{Cu}_2\text{FeSnS}_4$  (in stannite) +  $\text{ZnS}$  (in sphalerite) =  $\text{Cu}_2\text{ZnSnS}_4$  (in stannite) +  $\text{FeS}$  (in  
586 sphalerite). We have used the  $\log K_D$ - $T$  relationship of Shimizu and Shikazono (1985) to calculate the formation temperature of  
587 the pair, which is portrayed in the  $(X_{\text{Cu}_2\text{FeSnS}_4}/X_{\text{Cu}_2\text{ZnSnS}_4})-(X_{\text{FeS}}/X_{\text{ZnS}})$  plot of Shimizu and Shikazono (Fig. 11b). The resulting 220-  
588 305 °C interval lies at the low end of, or slightly outside, the 250-350 °C interval of the geothermometer.

589 Therefore, we ~~consider here~~ the 250-305 °C interval ~~can be taken as an estimation of the formation T of sphalerite-stannite in the~~  
590 ~~stylolite, the 220-250 °C interval should be taken with caution, as an~~ best estimation of the formation T of sphalerite-stannite  
591 ~~in the stylolite.~~

592

## 593 5 Discussion

594 Our work constrains the ~~structural~~ architecture and the environmental conditions at which BFZ300 deformation took place. Field  
595 and petrographic observations support the idea of transiently elevated fluid pressures, cyclic frictional-viscous deformation and  
596 progressive, yet discrete strain localization (Figs. 2, ~~and~~ 3). Analytical data suggest that these deformation cycles took place at  
597 the BDTZ. In the following, we discuss these constraints by systematically considering our different analytical results.

### 598 5.1. Fluid inclusion data and mineral-pair geothermometry

599 ~~Field evidence combined with microstructural observations, fluid inclusion analyses and the documented distinct generations of~~  
600 ~~synkinematic chlorites confirm that Qtz I and Qtz II veins precipitated from distinct generations/batches of aqueous fluid (i.e.~~  
601 ~~H<sub>2</sub>O-NaCl) pulses, repeatedly and actively injected into that ingressed the BFZ300 fault zone during different stages of its~~  
602 ~~evolution. Microthermometric results suggest that these fluids were in a homogeneous liquid state at the time of entrapment, as~~  
603 ~~testified by the consistent final homogenization into the liquid phase (i.e. by bubble disappearance).~~

604 ~~Microthermometric and Raman spectrometry data show that the fluid entrapped within the studied FIAs at the time of formation~~  
605 ~~of the damage zone and fault core during precipitation of Qtz I and Qtz II veins can be represented by a H<sub>2</sub>O-NaCl model fluid.~~  
606 ~~The fluid was in a homogeneous state at the time of entrapment, as testified by the consistent final homogenization by bubble~~  
607 ~~disappearance. It also had a low bulk salinity, as shown by the distribution of >80% of the ice melting ( $T_{\text{mice}}$ ) measurements~~  
608 ~~skewed towards values of -3 °C or higher, which corresponds to bulk salinities of 5 wt% NaCl<sub>eq</sub> or less (Fig. 10a-d).~~

609 ~~We documented a wide range of bulk salinity range in for~~ each FIAs entrapped within ~~the~~ quartz veins in each structural domain  
610 (Figs. 10a-d-e-g). ~~This suggests post-entrapment re-equilibration of fluid inclusions (cf. Bakker and Jansen, 1990; Diamond et~~  
611 ~~al., 2010). The  $T_{\text{hot}}$  varies between c. 130 and 440 °C without a clear mode or a skew (Figs. 10e-h-h) ~~indicating and shows that~~~~

612 no common range of entrapment temperatures can be identified in the dataset. Therefore, ~~we conclude that even~~ the properties of  
613 ~~individual,~~ petrographically intact FIAs do not correspond ~~with to~~ chemically well-preserved assemblages. Indeed, the ranges of  
614 ~~T<sub>tot</sub>~~ in individual FIAs are typically of the order of 150-200 °C (Figs. ~~10e-h~~), i.e. a value that is much higher than the ~10  
615 °C range expected for homogeneous FIAs entrapped isochorically and isoplethically (Fall et al., 2009; Vityk and Bodnar, 1998)  
616 and that demonstrates post-entrapment re-equilibration (cf. Vityk and Bodnar, 1998; Bodnar, 2003b; Sterner and Bodnar, 1989;  
617 Invernizzi et al., 1998). A major implication of fluid inclusion re-equilibration in our study is that the calculated fluid properties  
618 do not rigorously reflect those of the pristine fluid originally entrapped within BFZ300, but rather that of a fluid that modified its  
619 properties during the fault activity. ~~This is comparable to the results of other fluid inclusions studies from faults (Boullier, 1999;~~  
620 ~~Garofalo et al., 2014; Roedder, 1984).~~

621 Then, a possible approach to interpret our FI dataset is the comparison with the experimental work on synthetic fluid inclusions  
622 subjected to a range of post-entrapment re-equilibration conditions (Bakker, 2017; Bakker and Jansen, 1990, 1991, 1994; Vityk  
623 and Bodnar, 1995, 1998; Vityk et al., 1994; Invernizzi et al., 1998). ~~Such comparison~~ A straight comparison to the experiments is  
624 in our case difficult because most experimental work was carried out at high TP conditions (500-900 °C; 90-300 MPa) and also  
625 only few experiments were carried out under deviatoric stress conditions that approach those of natural rocks (Diamond et al.,  
626 2010; Tarantola et al., 2010). Despite these limitations, however, some key experimental results provide fundamental constraints  
627 on our dataset. First, both hydrostatic and uniaxial compression experiments showed that in each re-equilibrated FIA a number  
628 of inclusions survive virtually intact the modified post-entrapment PT conditions, showing that only severe deformation brings  
629 to total re-equilibration and complete obliteration of pristine inclusions (i.e.,  $\Delta\sigma > 100$  MPa in uniaxial compression experiments;  
630  $> 400$  MPa change of confining P in hydrostatic experiments). Second, under conditions leading to only low to moderate re-  
631 equilibration, the bulk chemical composition of the fluid inclusions does not change significantly from that of the pristine  
632 inclusions.

633 All of this implies that natural quartz samples with microstructures typical of moderate T deformation, such as deformation  
634 lamellae, deformation bands, undulose extinction and bulging, and hosting FIAs with moderately re-equilibrated textures, should  
635 still contain a number of inclusions whose properties resemble those of the pristine fluid. ~~In this scenario, our microthermometric~~  
636 ~~dataset can be used to constrain the more probable salinity ranges of the fluid batches which trigger BZ300 reactivation stages.~~  
637 ~~Two possible interpretations of the microthermometric dataset can be follow and we can give accordingly different salinity ranges~~  
638 ~~for the fluids.~~

639 ~~One possibility is that the different quartz veins and the fluids trapped within the fluid inclusions originated from multiple pulses~~  
640 ~~of a single, low-to-intermediate salinity fluid, with a salinity between 0 and 7 wt% NaCl<sub>eq</sub>, as shown by the distribution of >70%~~  
641 ~~of the bulk salinities skewed towards values of 7 wt% NaCl<sub>eq</sub> or less (Fig. 10a-d).~~ Thus, it is possible that ~~an~~ aliquots of the ~~40-~~  
642 ~~75 wt% NaCl<sub>eq</sub> FIAs from Qtz I and II crystals from both the damage zone and fault core is still representative of the pristine~~  
643 ~~sampled fluid. These inclusions would be those that survived or were relatively less affected by deformation events postdating~~  
644 ~~their entrapment. Inclusions falling outside the most typical 40-5-7wt% NaCl<sub>eq</sub> salinity range would instead correspond to those~~  
645 ~~which progressively modified their properties as a consequence of fluid-rock interaction during faulting and to those that~~

Formattato

Codice campo modificato

Formattato: Colore carattere: Rosso, Controllo ortografia e grammatica

646 experienced significant H<sub>2</sub>O loss and consequent salinity increase during the successive stages of fault deformation (cf. Bakker  
647 and Jansen, 1990; Diamond et al., 2010). The large documented range of T<sub>hot</sub> lacking a specific mode observed in individual  
648 FIAs is the product of fluid density changes caused by fluid inclusion re-equilibration during post-entrapment deformation. This  
649 would have happened repeatedly and cyclically within the host quartz during all ductile and brittle stages of deformation of the  
650 multi-stage deformation history of BFZ300.

651 Alternatively, multiple batches of fluids with different salinities (from low to intermediate salinity) may have ingressed and  
652 evolved within BFZ300 during its activity. In fact, considering the salinity dataset presented for each structural domain, fluid  
653 salinity can be seen clustering in restricted ranges typical for each domain: 1) the salinity of 60% of secondary fluid inclusions in  
654 Qtz I from the damage zone is between 0 and 1 wt%NaCleq; 2) > 80% of the secondary inclusions in Qtz I from the fault core  
655 preserve a salinity in the 1 to 5 range wt%NaCleq; 3) 75% of pseudosecondary inclusions in Qtz II show salinity values between  
656 6 and 11 wt%NaCleq and 4) ~70% of the secondary inclusions trapped within Qtz II show salinity values between 0 and 3  
657 wt%NaCleq. These clusters may best represent the original compositional ranges of different batches of fluids, each involved  
658 during a different faulting stage. Salinities outside these clusters may instead be explained again as resulting from the post-  
659 entrapment re-equilibration of those fluids with different salinities. This hypothetical scenario, in which chemically distinct fluids  
660 ingressing the fault and interacting with the rock at different times (e.g. Selverstone et al., 1992; Boiron et al., 2003; Famin et al.,  
661 2005) is also reinforced by several lines of observation such as: the variation of chlorite composition, the slight change in  
662 paragenesis/redox state with Quartz II and Quartz I (i.e. the absence of massive sulphides) and by the prolonged history of faulting  
663 (see below).

664 Fully aware of these interpretative uncertainties of our dataset ~~limitations~~, we have combined the microthermometric data of the  
665 studied FIAs with the independent quartz-chlorite and sphalerite-stannite geothermometers to constrain the most probable fluid  
666 pressure during the faulting events. With this approach, we use the formation temperatures of the mineral pairs as independent  
667 geothermometers and consider the intersection between these values and the FIA isochores to derive the ranges of trapping  
668 pressure (cf. Roedder and Bodnar, 1980). In Fig. 12, we present the Pf ranges that are calculated using the entire salinity range of  
669 the studied FIAs (cf. Fig. 10); however, we highlight the most probable Pf ranges that are consistent with what we consider best  
670 preserved salinity range (0-5 wt% NaCleq). Accordingly, for the damage zone we estimate a Pf interval of 20-90 MPa (Fig.12a)  
671 by intersecting the range of T obtained from the chlorite-quartz pair in the damage zone Qtz I (T c.170-240 °C, Fig. 11a) with the  
672 range of isochores from the same quartz. As to fluid pressure estimations in the fault core, we combine the 350 °C obtained from  
673 the chlorite-quartz pair from the fault core Qtz I (T>350 °C are outside the calibrated range of the geothermometer) with the  
674 ranges of isochores from the same quartz, from which we obtain Pf ranging between c. 140 and 120 MPa (Fig. 12b). Similarly,  
675 the intersection between the equilibrium T of the sphalerite-stannite pair in the Qtz II fault core (250-305 °C) and the range of  
676 isochores of the Type PS FIAs of Qtz II (Fig.9) defines Pf values ranging between 10 and 140 MPa (Fig.12c). Estimations from  
677 Type S4 FIAs (Fig.9) constrain a range between 40 and 160MPa (Fig. 12d). We propose that these values are sufficiently accurate  
678 to constrain multiple stages of fault slip, each one triggered by a fluid pulse having a distinct pressure. Hence, fault activity started

679 at 200 °C and at Pf varying between 20 and 90 MPa and continued through higher temperatures (305–350 °C) and Pf (120–160  
680 MPa).

681 In Figure 12, we present the ranges of the possible fluid pressure ( $P_f$ )s of the fluids involved during faulting as  $P_f$  calculated by  
682 combining from the fluid inclusion analysis data and with constrained the constraints by provided by the pair-mineral  
683 geothermometry and the hydro- and lithostatic pressure gradients and a possible geothermal gradient reconstructed regional  
684 geothermal gradients (e.g. Van Noten et al., 2011; Selverstone et al., 1995; Jaques and Pascal, 2017). The reconstructed regional  
685 gradients present at the time of vein emplacement are derived related from peak metamorphic conditions (4–5 kbar; 650–700 °C  
686 leading to c. 40 °C/km; from Kärki and Paulamäki, 2006). We used the geothermal gradient Hydrostatic and lithostatic pressures  
687 are then calculated by using pure water density and assuming a rock density of 2700 kg m<sup>-3</sup>, respectively, to calculate the hydrostatic  
688 and lithostatic pressure assuming a rock density of 2700 kg m<sup>-3</sup>. These gradients are used to give constrain the upper and lower  
689 bounds to physically possible fluid pressures. We computed the maximum and minimum isochores calculated by using the entire  
690 salinity and  $T_{hot}$  ranges obtained for from the FIAs in each structural domain (cf. Fig. 10). We also computed the isochores of the  
691 inclusions with the most representative salinity estimates evaluate for each structural domain, that we considered as indicative  
692 of the most probable active fluid phase obtained by. To estimate the most probable compositions of the distinct batches of fluids  
693 we were determined comparing the frequency diagrams (Fig. 10) with the and  $T_{hot}$  vs. salinity plots (see Supplementary  
694 Materials Fig. S4). Considering the peak temperature of each structural zone obtained from the geothermometric estimations  
695 combined in combination with the computed isochores, the estimated peak conditions of the fluid pressure are: 1) 80 MPa for Qtz  
696 I from the damage zone, 2) 210 MPa for Qtz I from the fault core-Qtz I; 3) 140 MPa from pseudosecondary inclusions in Qtz II  
697 from the core and 4) 180 MPa from secondary inclusions in Qtz II, still from the core (Fig. 12; Table 1).

698 In addition to the  $P_f$  peak conditions we can also constrain the physically possible other possible fluid pressure ranges for each  
699 stage of fluid ingress, which are given derived by considering the temperature range estimated for each structural domain. These  
700 pressure may be interpreted as the result of re-equilibration and progressive reactivation of the system recorded both by fluid  
701 inclusions and geothermometric estimations on authigenic minerals. Accordingly, Thus, for the damage zone, we estimate a  $P_f$   
702 interval of 50–80 MPa (Fig. 12a) can be derived by intersecting the range of T obtained from the chlorite-quartz pair in the Qtz I  
703 from the damage zone-Qtz I ( $T = 175–240$  °C, Fig. 11b) with the range of isochores from the same quartz. As to fluid pressure  
704 estimations in the fault core, we combine the 350 °C constraint obtained from the chlorite-quartz pair from Qtz I in the fault core  
705 Qtz I ( $T > 350$  °C are outside the calibrated range of the geothermometer) with the ranges of isochores from the same quartz, from  
706 which we obtain which yields  $P_f$  ranging between c. 30 and 210 MPa (Fig. 12b). Similarly, the intersection between the equilibrium  
707 T of the sphalerite-stannite pair in the Qtz II from the fault core (250–305 °C) and the range of isochores of the pseudosecondary  
708 FIAs of Qtz II (Type PS, Fig. 9g) defines  $P_f$  values ranging between 50 and 140 MPa (Fig. 12c). Estimations from secondary  
709 FIAs in Qtz II (Type S4, Fig. 9i) constrain a range between 40 and 180 MPa (Fig. 12d).

710 As also illustrated supported by the microstructures described above, we propose that these values are sufficiently accurate to  
711 constrain at least four stages of fault reactivation, each one triggered by a fluid pulse having a with distinct physico-chemical  
712 conditions physical and compositional properties.

713 ~~As suggested shown by the pressure-T vs. P plots of Figure 12, the secondary FIAs entrapped in Qtz I from the damage zone~~  
714 ~~show constrain the lowest value of  $P_f$  (i.e. 50-80 MPa) in of the entire dataset. We interpreted this not as representative of the~~  
715 ~~early BFZ300 localisation, but rather as the possible result of possibly resulting from -fluid entrapment during the latesta later~~  
716 ~~stages- of fault activityreactivation at  $T_f$ - occurred at lower temperature (~200 °C). This is also also-consistent with the estimated~~  
717 ~~calculated temperature of crystallization of the formation range of vermicular chlorite associated with Qtz I from the damage~~  
718 ~~zone (175-240 °C, Fig. 11b) and with the secondary nature of the entrapped FIAs. Also, the most abundant salinities observed in~~  
719 ~~the Qtz I from the damage zone (0-1 wt%NaCleq) coincide with the lowest  $T_{hot}$  measured in the same structural domain. The~~  
720 ~~latest-Later ffracturing of Qtz I in the damage zone were-may thus have been coeval -correlated-with the formation of vermicular~~  
721 ~~chlorite preserved therein, which is generally arrangedfound along secondary cracks and median lines (Fig. 5d).~~  
722 ~~In-the light of -all-these considerations, we interpreted-propose that initial BFZ300 localization occurred fault activity started in~~  
723 ~~the presence of a fluid with  $T_f$  and  $P_f$  of at - at least 350 °C or even higher temperature and at  $P_f$  probably higher than 210 MPa,~~  
724 ~~respectively. Later faulting and-continued by cyclic brittle-ductile switches induced and assisted by fluid batches through att~~  
725 ~~progressively lower-progressively lower temperatures and fluid pressure.~~

## 726 **5.2. Structural evolution and fluid flow: a conceptual model**

727 ~~BTherefore, bBased on the integration of-our field, microstructural, thermometric and fluid inclusions constraints (summarized~~  
728 ~~in- Table 1), we propose a conceptual model for the structural evolution of BFZ300 (Fig. 13). The fault's finite strain results from~~  
729 ~~several slip episodes mediated by multiple events of fluid ingress and fluid-rock interaction. A first constraint provided by our~~  
730 ~~study is that the analysis of the bulk chemical composition of the fluids that repeatedly cycliclycally flowed within-ingressed the fault~~  
731 ~~aresuggests characterized by specific values of  $T_f$ ,  $P_f$  and salinity, did not change significantly during the documented fault activity,~~  
732 ~~as the best preserved 0-5 wt% NaCleq salinity range points to a compositionally homogeneous fluid. This suggesting the likcly~~  
733 ~~presence of several a-batches of fluids of varying salinity and compositione compositionally heterogeneous-homogeneous source~~  
734 ~~region of the fluids-, which also their own evolve and modify their properties as the results of fluid-rock or, alternatively, that the~~  
735 ~~studied section of the fault did not interactions, with fluids of substantially different composition.~~

736 The embrittlement of the Olkiluoto metamorphic basement (time  $t_1$  of Figs.g- 13a, b) represents the initial stage of the  
737 deformational history of BFZ300, when conditions for brittle dilation and fracturing of the Paleoproterozoic basement were first  
738 met in a transient fashion. We propose that brittle failure under still ductile environmental conditions was caused by transiently  
739 elevated  $P_f$  (> 210 MPa) (probably under peak pressure major than 210 MPa), as also demonstrated by field evidence of  
740 hydrofracturing (pure tensional en echelon veins at the BDTZ depth, Figs. 2 and 3), and high fluid temperature (~350 °C or  
741 even higher), and the pore pressure estimations (Fig. 12 and Table 1). Hydrofracturing of the host basement is also expressed  
742 indicated by the emplacement of Qtz I veins along-within the diffuse network of joints and conjugate hybrid/shear fractures of  
743 the damage zone (Figs. 13a, -and-3a, b2g). These brittle features are quite evenly-broadly distributed within the damage zone  
744 suggesting an initial volumetrically diffuse strain distribution. Their formation caused the overall mechanical weakening of the

745 actively fracturing host rock volume, which in turn facilitated later strain localization. Brittle structures formed during this stage  
746 are discordant to the ENE-WSW striking metamorphic foliation (Fig. 1b), which they cut at high angle (Fig. 13a). Conditions for  
747 tensional and hybrid failure require low differential stress, i.e.  $\sigma_1 - \sigma_3 \sim 4T$ , where T is the tensional strength of the rock. Opening  
748 of fractures caused a stress drop, sudden increase of permeability, fluid venting and inhibited further build-up of P. Dilatant  
749 fractures were partially infilled by Qtz I, which precipitated from a first pulse of the low salinity fluid, with inferred low salinity  
750 (in the range between 1 and 5 wt% NaCl eq fluid for comparison with the salinity estimated from Qtz I fault core).  
751 Precipitation/Crystallization of Qtz I and formation of veins within these fractures caused hardening of the system. The progressive  
752 recovery of shear stresses concomitant with the progressive sealing of dilatant fractures altered the overall background stress  
753 conditions such that failure, after causing initial pure dilation, was later accommodated by hybrid extensional failure and,  
754 eventually, by shear fracturing (Fig. 13b), thus forming laterally continuous and interconnected shear fractures associated to with  
755 breccia pockets and cataclases (Figs. 3d, g, i) 2e-g-i and 3bd). Conjugate shear fractures connected the previously formed  
756 extensional fractures through a fracture coalescence mechanism (e.g. Griffith, 1921; Sibson, 1996); fracture coalescence  
757 mechanism in Qtz I is showed by a straight, red line in Fig. 13a). At the micro-scale this is demonstrated by the elongated blocky  
758 texture of Qtz I crystals from the damage zone (Figs. 4c and 5a11), where crystals grew at high angle to the vein boundaries (thus  
759 suggesting initial near-orthogonal dilation) and are physically connected by cataclastic shear bands to form a fault-fracture mesh  
760 (e.g. Sibson, 1996; Figures 4ab). Cataclastic bands formed at the expenses of the migmatitic host rock are enriched in authigenic,  
761 synkinematic sericite, likely due to the interaction between K-feldspar and fluids circulating in the dilatant fault zone (Fig. 4b).  
762 Shear fractures thus deformed the migmatitic host rock to connect dilatant and mostly Qtz I-filled tension gashes during a  
763 continuum of deformation. The conjugate shear fractures ascribable to this stage invariably define tight acute angles (Figs. 2b,  
764 3a), which we take as further evidence of overall low differential stress conditions at the time of failure (Fig. 13b).  
765 In synthesis, Qtz I veins from the damage zone are interpreted as the expression of the earliest stage of fault nucleation, before  
766 strain localization affected a progressively narrower rock volume to eventually form the main fault core. Indeed, the meso- and  
767 microscale features observed in Qtz I in the damage zone, lacking of pervasive crystal-plastic recrystallization deformation as  
768 otherwise occurred in Qtz I-fault core, are used to document the initial stage of embrittlement, preserves mostly brittle  
769 microstructure, with that hereby and lacks a pervasive ductile overprint, which is instead prevalent within the fault core. As a  
770 consequence, we interpret the chemical properties of the fluid derived from these veins as the closest to the initial conditions of  
771 the first fluid involved in BFZ300 nucleation. Fluid inclusion and geothermometric estimations from the synkinematic chlorite  
772 crystals associated with the damage zone Qtz I (Figs. 5a and 11a), suggest chlorite precipitation at a T of c. 200°C and P, between  
773 c. 90 and 20 MPa at the time of fault nucleation. Based on geometric, kinematic and deformation style characteristics, we  
774 tentatively assign this deformation episode to Stage 1 by Mattila and Viola (2014) (their Fig. 18), i.e. to a discrete brittle episode  
775 that they consider considered the expression of the earliest onset of brittle conditions in southwestern Finland c. 1.75 Ga ago,  
776 under overall NW-SE to NNW-SSE transpressive conditions.  
777 Further deformation of the BFZ300 (time  $t_2$  of Fig. 13c) occurred by progressive inward strain localization and narrowing of the  
778 actively deforming volume of the deformation zone (from a wide damage zone to a narrow fault core). The early BFZ300 core,



779 consisting of the main Qtz I vein is interpreted as having formed at this stage, within an overall dextral strike-slip kinematic  
780 framework. Emplacement of the Qtz I vein in the core represents the last pulse of this brittle deformational episode (Fig. 13b).  
781 Major fluid venting was likely associated with it, such that the system, once brittle failure in the core had occurred by  
782 hydrofracturing, moved back to a more diffuse deformation style typical of the still prevailing ductile conditions. Microscopic  
783 evidence of ductile-crystal-plastic deformation by-and dynamic recrystallization (Figs. 6-a, -b, Table 1) overprinting the early  
784 brittle structures of Qtz I in the fault core supports slow strain rate conditions during deformation. However, this viscous-ductile  
785 background deformation was punctuated by renewed and cyclically transient embrittlement as documented by healed fractures  
786 shown by trails of secondary fluid inclusions cutting across both the ductile fabrics and the earlier brittle deformational features  
787 (Figs. 6c, -d, -e). In accordance, EBSD results performed on analysis of the new grains documented along healed microcracks  
788 also suggests that they likely nucleated from fluids circulating in the early fractures before being later deformed result from quartz  
789 deformation in the low-temperature plasticity regime. In such regime, Thus, we show that at the BDTZ 'neocrystallisation' by  
790 nucleation and growth in fractured fragments and dynamic recrystallisation (typically by bulging and subgrain rotation) and  
791 'neocrystallisation' by nucleation and growth in fractured fragments coexist and compete in the overall microstructural evolution  
792 of quartz (e.g. Kjoll et al., 2015). Accordingly, the microstructures showed in Qtz I from the fault core show evidence for both  
793 processes being active during deformation of Qtz I grains. Initial nucleation from circulating fluids along now sealed cracks is  
794 proposed to have caused fracture healing and sealing. At the same time, and in light of targeted EBSD analysis that we have  
795 performed to better understand Qtz I crystallization in the fault core (see below), we can also document the local importance of  
796 dynamic recrystallisation by bulging and subgrain rotation. The combination of both mechanisms recalls the results by Kjoll et  
797 al. (2015), which proposed the combination of these mechanisms after a detailed microstructural analysis in quartz veins  
798 associated with a thrust, formed at the brittle ductile transition. Repeated pulses of high P<sub>i</sub> (peak conditions: 210-20-140 MPa)  
799 likely triggered these brittle-ductile oscillations. Repeated fluid ingresses and related deformation would, in addition, also have  
800 caused some of the post-entrapment equilibration of the FI, as discussed above.

801 The cycles of brittle and viscous deformation may be explained as follows. Cyclic brittle failure would have repeatedly lowered  
802 P<sub>i</sub>, which lowered the background stress and strain rate and favoured ductile deformation by dynamic recrystallization at T > 300  
803 °C between the slip events (e.g. Passchier and Trow, 2005). The fault regained cohesive strength after each brittle failure episode  
804 through vein formation and sealing/healing of the fracture networks. Porosity destruction by mineral crystallization and fracture  
805 sealing, as clearly shown by CL imaging (Fig 4d), induced a progressive reduction of permeability and mechanical healing of the  
806 fault, which promoted an increase of P<sub>i</sub> and ultimately triggered a new brittle failure. Therefore, pore pressure build-up promoted  
807 episodic brittle fracturing followed by cementation and plastic deformation/recovery. The compelling evidence for this  
808 deformation occurring at T ≈ 350° C indicate that the described processes identify the BDT of the quartz-feldspathic crust  
809 (Kohlstedt et al., 1995).

810 Mattila and Viola (2014) described a second brittle stage (referred to as Stage 2, their Fig. 18) during which a c. N-S to NNE-  
811 SSW-oriented episode of transpressional deformation affected southwestern Finland. Geometric and temporal relationships  
812 between structures of Stages 1 and 2 (see also Viola et al., 2009) were used to infer a clockwise rotation of the horizontal

813 compression direction from NW-SE (Stage 1) to NNE-SSW (Stage 2). Consistent with the kinematic framework of Stage 2, we  
814 propose here that during progressive regional exhumation and cooling to entirely brittle conditions, the BFZ300 deformation  
815 continued through a further, distinct deformation phase ( $t_3$  of Fig. 13c). This stage accommodated the selective reactivation of the  
816 BFZ300 core, with renewed dilation due to the rotated  $\sigma_1$  during Stage 2 acting subparallel to the strike of the Qtz I vein in the  
817 BFZ300 core. Localised dilation in a still fluid-rich system allowed the emplacement of the Qtz II vein (Fig. 13e). Our estimations  
818 indicate ~~that peak conditions of  $P_f$  and T conditions at that time were 140 between 140 and 10 MPa and  $T \approx 305^\circ\text{C}$ , respectively.~~  
819 The BFZ300 core was reactivated by an intermediate salinity fluid (in the range between 6 and 11 wt%NaCl<sub>eq</sub>) under overall  
820 hybrid conditions (Fig. 13f), as suggested by the irregular thickness and curved geometry of the Qtz II vein therein, and by the  
821 synkinematic chlorite crystals that are stretched orthogonally to the vein boundaries (Fig. 3he). The Qtz II vein invariably  
822 localized along at the contact between Qtz I and the host rock (Figs. s.3f, 2, 3 and 13c) suggesting selective reactivation along  
823 the pre-existing principal slip zones (Riedel shears and boundary shears, Tchalenko, 1970), which represented the weakest part  
824 of the fault (strength profile Fig. 13h). Evidence for mesoscale hybrid fracturing and our  $P_f$  estimates (Fig. 112) suggest that  $P_f$   
825 was lower than that of the earlier deformation stages during Qtz I emplacement.  
826 BFZ300 underwent one or more events of brittle fracturing and induration (Fig. 13g), as suggested by the CL imaging of Qtz II  
827 crystals (Fig. 7c). The fluid pressure peak value estimations for this structural stage is around c. 180 phase are between 160 and  
828 40 MPa.  
829 A possible latest, very late BFZ300 reactivation stage (time,  $t_3$ ), of unknown age is also documented by the secondary chlorite  
830 associated with Qtz I in the damage zone (Figs. 5a, d). The lowest temperature estimated from chlorite geothermometry ( $\sim 200^\circ\text{C}$ ),  
831 consistent with the lowest homogenization temperature of the greatest part of FIAs petrographically discriminated in this  
832 structural domain, suggest that they probably represent a latest reactivation of the system, triggered by a batch of fluid with at  
833 lower temperature ( $\sim 200^\circ\text{C}$ ), lower pressure (peak conditions: 80 MPa) and lower salinity (0.1 wt%NaCl<sub>eq</sub>). This deformation  
834 stages may probably be not consistent with the deformation cycle here presented.  
835 ~~Also,~~ the stylonitic seams having a strike striking parallel to the BFZ300 fault zone suggest a direction of maximum compression  
836 ( $\sigma_1$ ) oriented c. E-W, i.e. subparallel to the inferred Sveonorwegian main shortening direction (e.g., Viola et al., 2011). The  
837 sphalerite-stannite mineral pairs arranged along these structures are supposed to be were possibly concentrated through a pression-  
838 solution mechanism during this deformational stage.  
839 Skyttä and Torvela (2018) proposed that the BFZ300 is a brittle structure localized onto a zone of incomplete structural  
840 transposition inherited from the earlier ductile history of the Olkiluoto basement. However, in our mesoscale and microstructural  
841 analysis we did not find evidence of any ductile precursor, and we note that BFZ300 cuts the ductile structural grain at high angle,  
842 which excludes any reactivation of precursor ductile fabrics.

### 843 5.3. Implications for seismic deformation at the base of the BDTZ

844 This study demonstrates the role of overpressured fluids on strain localisation during the incipient stages of fault nucleation and  
845 subsequent reactivation(s) at the BDTZ. The maximum estimated ~~fluid pressure~~ $P$  and ~~fluid temperature~~ $T$  conditions derived in  
846 this study (peak conditions of ~~210+60~~ MPa and 350 °C) are indeed realistic for the base of the seismogenic zone in the continental  
847 lithosphere (e.g., Scholz, 1990, and references therein) where the brittle-ductile transition for quartz occurs.

848 Mechanical models of long-term deformation (Rolandone and Jaupart, 2002) propose that deformation at the brittle-ductile  
849 transition can be reasonably described as being mostly accommodated by intermittent and concomitant coseismic slip and ductile  
850 flow. ~~Major~~ hydrofracturing, as that documented in this study by the Qtz I and II veins, is possibly related ~~in that context~~ to  
851 seismic failure. Faults accommodating hydrofracturing are indeed commonly interpreted as seismogenic (e.g. Sibson, 1992a;  
852 Cox, 1995) particularly at depth, ~~where the reactivation of misoriented faults is only possible for fluid pressures exceeding  $\sigma_3$~~   
853 ~~(e.g. Sibson, 1985).~~

854 Our study confirms this view because BFZ300 contains not only brittle fault rocks overprinting and overprinted by veins, but also  
855 clearcut evidence of mutually overprinting brittle and ductile deformation (Fig. 6). In ~~the~~ light of the field observations discussed  
856 and of the constraints derived, we suggest therefore that BFZ300 behaved in a seismic way at least during the emplacement of  
857 the principal Qtz I and Qtz II veins. ~~Hydrofracture veins are largely interpreted in the literature as the evidence of earthquake in~~  
858 ~~fluid-rich faults (Cox, 1995).~~

859 In this perspective, two possible scenarios can be considered to explain the genetic relationships between BFZ300 and a possible  
860 seismic behaviour of the crust during the Svecofennian orogeny. In a first scenario, the quartz veins of the fault core would  
861 represent the result of coseismic rupture during the mainshocks of a fully developed seismic cycle. Pore pressure fluctuations  
862 caused the repeated transient embrittlement of the rock mass, ~~which~~ was otherwise under overall ductile conditions. The  
863 documented brittle-ductile cycles are thus the expression of coseismic fracturing and aseismic creep between the individual  
864 shocks, as shown by viscous deformation overprinting the brittle features, guided by the residual differential stress.

865 A second possibility is that faulting occurred in the absence of a well-defined sequence of main- and aftershocks. As in the case  
866 of man-induced earthquakes triggered by high-pressure fluids during injection of fluids (e.g. Healy et al., 1968), where  
867 deformation is typically accommodated by diffuse swarms of low magnitude seismicity rather than well-defined mainshock-  
868 aftershock sequences (Cox, 2016), we propose that BFZ300 might have localised strain by diffuse veining with crack and seal  
869 textures (Cox, 2016). Breccias and cataclasites (Fig.s ~~s~~ 3, ~~and~~ 8) mutually overprinting with veins show that failure and veining  
870 were indeed broadly coeval (e.g. Cox, 1995; Cox, 2016). Healing in fluid-rich environments can occur over short periods of time  
871 (days-months) when compared with recurrence time of large earthquakes (10-100 years) (Olsen et al., 1998; Tenthorey and Cox,  
872 2006). Therefore, the documented repeated switches between brittle and ductile deformations would then be steered again by  
873 transient episodes of fluid overpressuring but in this case would express the accommodation of swarms of minor background  
874 earthquakes within overall ductile conditions.

875 Microstructures of fault-rocks exhumed from the brittle-ductile transition in other geological settings, are mostly in agreement  
876 with our hypotheses of seismic deformation. Transient and short term high-stress deformation followed by phases of stress  
877 relaxation, which is prevalently characterized by recovery and recrystallization processes, has been documented by several  
878 authors in deformed quartz (Trepmann and Stöckhert, 2003; Trepmann et al., 2007; Bestmann et al., 2012; Trepmann and  
879 Stöckhert, 2013; Trepmann et al., 2017).

880 ~~To conclude, BFZ300 represents an interesting case of likely seismic deformation within a fluid rich system at the base of the~~  
881 ~~seismogenic crust. The absence of later, thoroughgoing and high-strain, potentially obliterating deformation episodes allows the~~  
882 ~~documentation of a complex structural evolution, from the earliest localisation to the mature structural stage.~~

## 883 6 Conclusions

884 ~~This work~~~~study~~~~Our analysis~~ shows that ~~a~~ ~~a~~-multi-scale ~~and~~~~disciplinary~~, multi-technique ~~approach~~, based on the  
885 ~~combination~~ leading to the generation of several independent constraints offers the potential to, ~~gives an high degree of confidence~~  
886 ~~when used to~~ ~~reconstruct~~ in detail the evolutionary history ~~evolution~~ stages of also ~~a~~ fault zones that, which have experienced  
887 multiple events of reactivation triggered by fluid overpressure and in which intense fluid-rock re-equilibration processes have  
888 taken place. In accordance, ~~We~~ documented the localised, initial embrittlement ~~stage~~ of the Olkiluoto-Paleoproterozoic  
889 basement of southwestern Finland at the BDTZ, which occurred by brittle-brittle failure under ~~still~~ overall ductile ~~environmental~~  
890 conditions caused by in response to transiently elevated high fluid pressure and temperature (peak conditions:  $P_f > 210$  MPa;  
891  $T \sim 350$  °C). ~~Latest events of reactivation and strain localization occurred by several brittle-ductile deformation cycles, triggered~~  
892 ~~again by multiple pulses of high pressure fluids channelled into the system.~~ study of faulting initiation and evolution has indeed  
893 the potential to provide useful insights into the complex and cyclic processes of fluid-fault interaction and effects thereof at the  
894 base of the seismogenic crust. ~~It~~ Our results further constrains, moreover, the importance of cyclic seismicity and fluids in the  
895 fragmentation of Precambrian cratons when deformed at the brittle-ductile transition zone ~~BDTZ~~, something that is not yet that  
896 well understood for the Fennoscandian Shield. Our study, moreover, provides potentially important inputs to many modern  
897 geological applications, including site characterization of deep geological disposal facilities for spent nuclear fuel. Results from  
898 the detailed geological characterization of faults at the Olkiluoto site can thus be used toward the continuous updating of the  
899 geological site description and yield further constraints on the mechanics of faulting at ~~the BDTZ~~ ~~those conditions and at that~~  
900 ~~time.~~

901

## 902 ACKNOWLEDGMENTS

903 ~~This research was partly funded by Posiva Oy. We thank Oliver Vanderhaeghe and two anonymous reviewers for their~~  
904 ~~constructive reviews, which led to a greatly improved manuscript. Stephen F. Cox, Michael Stipp and Alfons M. Van den Kerkhof~~  
905 ~~are all warmly thanked for fruitful discussions during the early stages of this work. Danilo Bersani and Andrea Risplendente are~~  
906 ~~also thanked for their help with the Raman and SEM analysis.~~

907 **References**

- 908 Aaltonen, I., Lahti, M., Engström, J., Mattila, J., Paananen, M., Paulamäki, S., Gehör, S., Kärki, A., Ahokas, T., Torvela,  
909 T. and Front, K.: Geological model of the Olkiluoto site, Version 2.0, Posiva Working Report 2010- 70, Posiva Oy,  
910 Eurajoki, 2010.
- 911 Aaltonen, I., Engström, J., Front, K., Gehör, S., Kosunen, P. and Kärki, A.: Geology of Olkiluoto. Posiva Working Report  
912 2016- 16., Posiva Oy, Eurajoki., 2016.
- 913 Andersen, T., Austrheim, H. and Burke, E. A. J.: Fluid inclusions in granulites and eclogites from the Bergen Arcs,  
914 Caledonides of W. Norway, *Mineral. Mag.*, 54, 145–158, 1990.
- 915 Ault, A. K. and Selverstone, J.: Microtextural constraints on the interplay between fluid-rock reactions and deformation,  
916 *Contrib. to Mineral. Petrol.*, 156(4), 501–515, doi:10.1007/s00410-008-0298-9, 2008.
- 917 Bakker, R.: Re-Equilibration Processes in Fluid Inclusion Assemblages, *Minerals*, 7(7), 117, doi:10.3390/min7070117,  
918 2017.
- 919 Bakker, R. J. and Jansen, J. B. H.: Preferential water leakage from fluid inclusions by means of mobile dislocations, *Nature*,  
920 345(6270), 58–60, doi:10.1038/345058a0, 1990.
- 921 Bakker, R. J. and Jansen, J. B. H.: Experimental post-entrapment water loss from synthetic CO<sub>2</sub>-H<sub>2</sub>O inclusions in natural  
922 quartz, *Geochim. Cosmochim. Acta*, 55(8), 2215–2230, doi:10.1016/0016-7037(91)90098-P, 1991.
- 923 Bakker, R. J. and Jansen, J. B. H.: A mechanism for preferential H<sub>2</sub>O leakage from fluid inclusions in quartz, based on  
924 TEM observations, *Contrib. to Mineral. Petrol.*, 116(1–2), 7–20, doi:10.1007/BF00310686, 1994.
- 925 ~~Barton, P. B. and Bethke, P. M.: Chalcopyrite disease in sphalerite: Pathology and epidemiology, *Am. Mineral.*, 72(5–6),  
926 451–467, 1987.~~
- 927 Basson, I. J. and Viola, G.: Passive kimberlite intrusion into actively dilating dyke-fracture arrays: Evidence from fibrous  
928 calcite veins and extensional fracture cleavage, *Lithos*, 76(1–4 SPEC. ISS.), 283–297, doi:10.1016/j.lithos.2004.03.041,  
929 2004.
- 930 Bestmann, M., Pennacchioni, G., Nielsen, S., Göken, M. and de Wall, H.: Deformation and ultrafine dynamic  
931 recrystallization of quartz in pseudotachylyte-bearing brittle faults: A matter of a few seconds, *J. Struct. Geol.*, 38, 21–38,  
932 doi:10.1016/j.jsg.2011.10.001, 2012.
- 933 Bodnar, R. J.: The origin of fluid inclusions, in: Samson, I., Anderson, A. & Marshall, D. (eds.) *Fluid inclusions: Analysis  
934 and Interpretation*. Vancouver, Canada: Mineralogical Association of Canada, 11-18, 2003a.
- 935 Bodnar, R. J.: Re-equilibration of fluid inclusions, in: Samson, I., Anderson, A. & Marshall, D. (eds.) *Fluid inclusions:  
936 Analysis and Interpretation*. Vancouver, Canada: Mineralogical Association of Canada, 213-230, 2003b.
- 937 Boiron, M., Cathelineau, M., Banks, D. A., Fourcade, S. and Vallance, J.: Mixing of metamorphic and surficial fluids  
938 during the uplift of the Hercynian upper crust: consequences for gold deposition, *Chem. Geol.*, 194, 119–141, 2003.

939 Bons, P. D.: The formation of large quartz veins by rapid ascent of fluids in mobile hydrofractures, *Tectonophysics*, 336(1–  
940 4), 1–17, doi:10.1016/S0040-1951(01)00090-7, 2001.

941 Bons, P. D., Elburg, M. A. and Gomez-Rivas, E.: A review of the formation of tectonic veins and their microstructures, *J.*  
942 *Struct. Geol.*, 43, 33–62, doi:10.1016/j.jsg.2012.07.005, 2012.

943 ~~Boullier, A. M.: Fluid inclusions: Tectonic indicators, *J. Struct. Geol.*, 21(8–9), 1229–1235, doi:10.1016/S0191-~~  
944 ~~8141(99)00039-5, 1999.~~

945 Bourdelle, F. and Cathelineau, M.: Low-temperature chlorite geothermometry: a graphical representation based on a T–  
946 R2+–Si diagram, *Eur. J. Mineral.*, 27(5), 617–626, doi:10.1127/ejm/2015/0027-2467, 2015.

947 Caine, J. S., Evans, J. P. and Forster, C. B.: Fault zone architecture and permeability structure, *Geology*, 24(11), 1025–  
948 1028, doi:10.1130/0091-7613(1996)024<1025, 1996.

949 Compton, K. E., Kirkpatrick, J. D. and Holk, G. J.: Cyclical shear fracture and viscous flow during transitional ductile–  
950 brittle deformation in the Saddlebag Lake Shear Zone, California, *Tectonophysics*, 708, 1–14,  
951 doi:10.1016/j.tecto.2017.04.006, 2017.

952 Cox, S. F.: Faulting processes at high fluid pressures: An example of fault valve behavior from the Wattle Gully Fault,  
953 Victoria, Australia, *J. Geophys. Res.*, 100(B7), 841–859, 1995.

954 Cox S. F.: Coupling between deformation, fluid pressures and fluid flow in ore-producing hydrothermal environments,  
955 *Econ. Geol.*, 100th Anniversary Volume, 39–75, 2005.

956 Cox, S. F.: Injection-driven swarm seismicity and permeability enhancement: Implications for the dynamics of  
957 hydrothermal ore systems in high fluid-flux, overpressured faulting regimes - An invited paper, *Econ. Geol.*, 111(3), 559–  
958 587, doi:10.2113/econgeo.111.3.559, 2016.

959 Cox, S., Knackstedt, M., & Braun, J.: Principles of structural control on permeability and fluid flow in hydrothermal  
960 systems, *Reviews in Econ. Geol.*, 14, 1–24, 2001.

961 Crider, J. G. and Peacock, D. C. P.: Initiation of brittle faults in the upper crust: A review of field observations, *J. Struct.*  
962 *Geol.*, 26(4), 691–707, doi:10.1016/j.jsg.2003.07.007, 2004.

963 De Paola, N., Collettini, C., Trippetta, F., Barchi, M. R. and Minelli, G.: A mechanical model for complex fault patterns  
964 induced by evaporite dehydration and cyclic changes in fluid pressure, *J. Struct. Geol.*, 29(10), 1573–1584,  
965 doi:10.1016/j.jsg.2007.07.015, 2007.

966 Derez, T., Pennock, G., Drury, M. and Sintubin, M.: Low-temperature intracrystalline deformation microstructures in  
967 quartz, *J. Struct. Geol.*, 71, 3–23, doi:10.1016/j.jsg.2014.07.015, 2015.

968 Diamond, L. W.: Introduction to gas-bearing, aqueous fluid inclusions, in : *Fluid Inclusions: Analysis and Interpretation*,  
969 edited by: I. Samson, A. Anderson, D. Marshall, eds., 363–372., 2003.

970 Diamond, L. W., Tarantola, A. and Stünitz, H.: Modification of fluid inclusions in quartz by deviatoric stress. II:  
971 Experimentally induced changes in inclusion volume and composition, *Contrib. to Mineral. Petrol.*, 160(6), 845–864,

972 doi:10.1007/s00410-010-0510-6, 2010.

973 Dubessy, J., Buschaert, S., Lamb, W., Pironon, J. and Thiéry, R.: Methane-bearing aqueous fluid inclusions: Raman  
974 analysis, thermodynamic modelling and application to petroleum basins, *Chem. Geol.*, 173(1–3), 193–205,  
975 doi:10.1016/S0009-2541(00)00275-8, 2001.

976 Ehlers, C., Lindroos, A. and Selonen, O.: The late Svecofennian granite-migmatite zone of southern Finland-a belt of  
977 transpressive deformation and granite emplacement., *Precambrian Res.*, 64(1–4), 295–309, 1993.

978 Fall, A., Donald, R. and Bodnar, R. J.: The effect of fluid inclusion size on determination of homogenization temperature  
979 and density of liquid-rich aqueous inclusions, *Am. Mineral.*, 94(11–12), 1569–1579, doi:10.2138/am.2009.3186, 2009.

980 [Famin, V., Hébert, R., Philippot, P. and Jolivet, L.: Evolution of hydrothermal regime along a crustal shear zone, Tinos  
981 Island, Greece, \*Tectonics\*, 23, doi:10.1029/2003TC001509, 2004.](#)

982 [Famin, V., Hébert, R., Philippot, P. and Jolivet, L.: Ion probe and fluid inclusion evidence for co-seismic fluid infiltration  
983 in a crustal detachment, \*Contrib. Mineral Petrol.\*, 150, 354–367, doi:10.1007/s00410-005-0031-x, 2005.](#)

984 Garofalo, P. S.: Mass transfer during gold precipitation within a vertically extensive vein network (Sigma deposit - Abitibi  
985 greenstone belt - Canada). Part II. Mass transfer calculations, *Eur. J. Mineral.*, 16(5), 761–776, doi:10.1127/0935-  
986 1221/2004/0016-0761, 2004.

987 Garofalo, P. S., Matthäi, S. K. & Heinrich, C. A.: Three-dimensional geometry, ore distribution, and time-integrated mass  
988 transfer through the quartz-tourmaline-gold vein network of the Sigma deposit (Abitibi belt - Canada), *Geofluids*, 2, 217-  
989 232, 2002.

990 Garofalo, P. S., Fricker, M. B., Günther, D., Bersani, D. and Lottici, P.: Physical-chemical properties and metal budget of  
991 Au-transporting hydrothermal fluids in orogenic deposits, *Geol. Soc. London, Spec. Publ.*, 402(1), 71–102,  
992 doi:10.1144/SP402.8, 2014.

993 Goddard, J. V. and Evans, J. P.: Chemical changes and fluid-rock interaction in faults of crystalline thrust sheets,  
994 northwestern Wyoming, U.S.A., *J. Struct. Geol.*, 17(4), 533–547, doi:10.1016/0191-8141(94)00068-B, 1995.

995 Goldstein, R. H. and Reynolds, T. J.: Fluid Inclusion Microthermometry, *Syst. Fluid Inclusions Diagenetic Miner.*, 87–  
996 121, doi:10.2110/scn.94.31.0087, 1994.

997 Gorbatshev, R. and Bogdanova, S.: Frontiers in the Baltic Shield, *Precambrian Res.*, 64(1–4), 3–21, doi:10.1016/0301-  
998 9268(93)90066-B, 1993.

999 Griffith, A. A.: The Phenomena of Rupture and Flow in Solids, *Philos. Trans. R. Soc. London*, 221(582–893), 163–198,  
1000 1920.

1001 Guerami, A. and Pennacchioni, G.: Brittle precursors of plastic deformation in a granite: An example from the Mont Blanc  
1002 massif (Helvetic, western Alps), *J. Struct. Geol.*, 20(2–3), 135–148, doi:10.1016/S0191-8141(97)00080-1, 1998.

1003 Healy, J. H., Rubey, W. W., Griggs, D. T. and Raleigh, C. B.: The Denver Earthquakes. Disposal of waste fluids by injection  
1004 into a deep well has triggered earthquakes near Denver, Colorado., *Science*, 161(3848), 1301–1310, 1968.

- 1005 Heinrich, C. A., Andrew, A. S., and Knill, M. D.: Regional metamorphism and ore formation: Evidence from stable isotopes  
1006 and other fluid tracers, *Reviews in Econ Geol*, 11, 97–117, 2000.
- 1007 [Hey, M. H.: A new review of the chlorites., \*Mineral. Mag. J. Mineral. Soc.\*, XXX\(224\), 1954.](#)
- 1008 [Hudson, J. A. and Cosgrove, J.: Geological History and Its Impact on the Rock Mechanics Properties of the Olkiluoto Site,  
1009 Posiva Working Report 2006, Posiva Oy, Eurajoki, 2006.](#)
- 1010 [Invernizzi, C., Vityk, M., Cello, G. and Bodnar, R.: Fluid inclusions in high pressure/low temperature rocks from the  
1011 Calabrian Arc \( Southern Italy \): the burial and exhumation history of the subduction-related Diamante-Terranova unit, \*J.  
1012 Metamorph. Geol.\*, 16, 2, 247–258, 1998.](#)
- 1013 [Jaques, L. and Pascal, C.: Full paleostress tensor reconstruction using quartz veins of Panasqueira Mine, central Portugal;  
1014 part I: Palcpressure determination, \*J. Struct. Geol.\*, 102, 58–74, doi:10.1016/j.jsg.2017.07.006, 2017.](#)
- 1015 Kaduri, M., Gratier, J. P., Renard, F., Çakir, Z. and Lasserre, C.: The implications of fault zone transformation on aseismic  
1016 creep: Example of the North Anatolian Fault, Turkey, *J. Geophys. Res. Solid Earth*, 122(6), 4208–4236,  
1017 doi:10.1002/2016JB013803, 2017.
- 1018 Kerrich, R.: Some effects of tectonic recrystallisation on fluid inclusions in vein quartz, *Contrib. to Mineral. Petrol.*, 59(2),  
1019 195–202, doi:10.1007/BF00371308, 1976.
- 1020 Kjöll, H. J., Viola, G., Menegon, L. and Sørensen, B. E.: Brittle-viscous deformation of vein quartz under fluid-rich lower  
1021 greenschist facies conditions, *Solid Earth*, 6(2), 681–699, doi:10.5194/se-6-681-2015, 2015.
- 1022 Kohlstedt, D. L., Evans, B. and Mackwell, S. J.: Strength of the lithosphere: Constraints imposed by laboratory  
1023 experiments, *J. Geophys. Res.*, 100(B9), 587–602, 1995.
- 1024 Korja, A., Heikkinen, P. and Aaro, S.: Crustal structure of the northern Baltic Sea palaeorift, *Tectonophysics*, 331(4), 341–  
1025 358, doi:10.1016/S0040-1951(00)00290-0, 2001.
- 1026 Kukkonen, I. T. and Lauri, L. S.: Modelling the thermal evolution of a collisional Precambrian orogen: High heat  
1027 production migmatitic granites of southern Finland, *Precambrian Res.*, 168(3–4), 233–246,  
1028 doi:10.1016/j.precamres.2008.10.004, 2009.
- 1029 [Kärki, A. and Paulamäki, S.: Petrology of Olkiluoto, Posiva Report 2006-02, Posiva Oy, Eurajoki., 2006.](#)
- 1030 Lahtinen, R. and Survey, G.: Palaeoproterozoic tectonic evolution of the Fennoscandian Shield. In: Lehtinen, M., Nurmi,  
1031 P.A., Rämö (eds.), *Precambrian Geology of Finland: Key to the Evolution of the Fennoscandian Shield*, Developments in  
1032 Precambrian Geology, 2005.
- 1033 Mancktelow, N. S. and Pennacchioni, G.: The influence of grain boundary fluids on the microstructure of quartz-feldspar  
1034 mylonites, *J. Struct. Geol.*, 26, 47–69, doi:10.1016/S0191-8141(03)00081-6, 2004.
- 1035 Mancktelow, N. S. and Pennacchioni, G.: The control of precursor brittle fracture and fluid-rock interaction on the  
1036 development of single and paired ductile shear zones, *J. Struct. Geol.*, 27(4), 645–661, doi:10.1016/j.jsg.2004.12.001, 2005.



- 1037 Mattila, J. and Viola, G.: New constraints on 1.7Gyr of brittle tectonic evolution in southwestern Finland derived from a  
 1038 structural study at the site of a potential nuclear waste repository (Olkiluoto Island), *J. Struct. Geol.*, 67(PA), 50–74,  
 1039 doi:10.1016/j.jsg.2014.07.003, 2014.
- 1040 Menegon, L., Pennacchioni G., Malaspina N., Harris K., and Wood E.: Earthquakes as Precursors of Ductile Shear Zones  
 1041 in the Dry and Strong Lower Crust, *Geochem. Geophys. Geosy.*, 18(12), doi: 10.1002/2015GC006010, 2017.
- 1042 Menegon, L., Marchesini, B., Prando, F., Garofalo, P. S., Viola, G., Anderson, M. and Mattila, J.: Brittle-viscous  
 1043 oscillations and different slip behaviours in a conjugate set of strike-slip faults, *Geophysical Research Abstracts Vol. 20*,  
 1044 EGU2018-14799, 2018.
- 1045 Miller, S. A.: *The Role of Fluids in Tectonic and Earthquake Processes*, edited by R. Dmowska, Elsevier., 2013.
- 1046 Mitterpergher, S., Dallai, L., Pennacchioni, G., Renard, F. and Di Toro, G.: Origin of hydrous fluids at seismogenic depth:  
 1047 Constraints from natural and experimental fault rocks, *Earth Planet. Sci. Lett.*, 385, 97–109,  
 1048 doi:10.1016/j.epsl.2013.10.027, 2014.
- 1049 [Moritz, R., Ghazban, F. and Singer, B. S.: Eocene Gold Ore Formation at Muteh, Sanandaj-Sirjan Tectonic Zone, Western](#)  
 1050 [Iran: A Result of Late-Stage Extension and Exhumation of Metamorphic Basement Rocks within the Zagros Orogen, \*Econ.\*](#)  
 1051 [Geol.](#), 101, 1–28, 2006.
- 1052 [Morrison, J.: Meteoric water-rock interaction in the lower plate of the Whipple Mountain metamorphic core complex ,](#)  
 1053 [California, \*J. Metamorph. Geol.\*, 12, 827–840, 1994.](#)
- 1054 [Morrison, J. and Anderson, J. L.: Footwall Refrigeration Along a Detachment Fault : Implications for the Thermal](#)  
 1055 [Evolution of Core Complexes, \*Science\*, 279\(January\), 63–67, 1998.](#)
- 1056 [Mulch, A., Mine, I. De, Cosca, M. A., Mine, I. De, Lausanne, D., Lausanne, C.-, Poincare, H. and Gr. U. M. R.:](#)  
 1057 [Reconstructing paleoelevation in eroded orogens. , \(6\), 525–528, doi:10.1130/G20394.1, 2004.](#)
- 1058 Nekrasov, I. J., Sorokin, V. I. and Osadchii, E. G.: Fe and Zn partitioning between stannite and sphalerite and its application  
 1059 in geothermometry., *Phys. Chem. Earth*, 11(C), 739–742, doi:10.1016/0079-1946(79)90069-7, 1979.
- 1060 Oliver, N. H. S. and Bons P. D.: Mechanisms of fluid flow and fluid–rock interaction in fossil metamorphic hydrothermal  
 1061 systems inferred from vein–wallrock patterns, geometry and microstructure, *Geofluids*, 137–162, 2001.
- 1062 Olsen, M. P., Scholz, C. H. and Léger, A.: Healing and sealing of a simulated fault gouge under hydrothermal conditions:  
 1063 Implications for fault healing, *J. Geophys. Res.*, 103(B4), 7421, doi:10.1029/97JB03402, 1998.
- 1064 Pennacchioni, G., Di Toro, G., Brack, P., Menegon, L. and Villa, I. M.: Brittle-ductile-brittle deformation during cooling  
 1065 of tonalite (Adamello, Southern Italian Alps), *Tectonophysics*, 427(1–4), 171–197, doi:10.1016/j.tecto.2006.05.019, 2006.
- 1066 Roedder, E. and Bodnar, R. J.: Geologic determinations from fluid inclusion studies., *Annu. Rev. Earth Planet. Sci.*,  
 1067 8(1953), 263–301, 1980.
- 1068 Rolandone, F. and Jaupart, C.: The distributions of slip rate and ductile deformation in a strike-slip shear zone, *Geophys.*  
 1069 *J. Int.*, 148(2), 179–192, doi:10.1046/j.1365-246X.2002.01574.x, 2002.

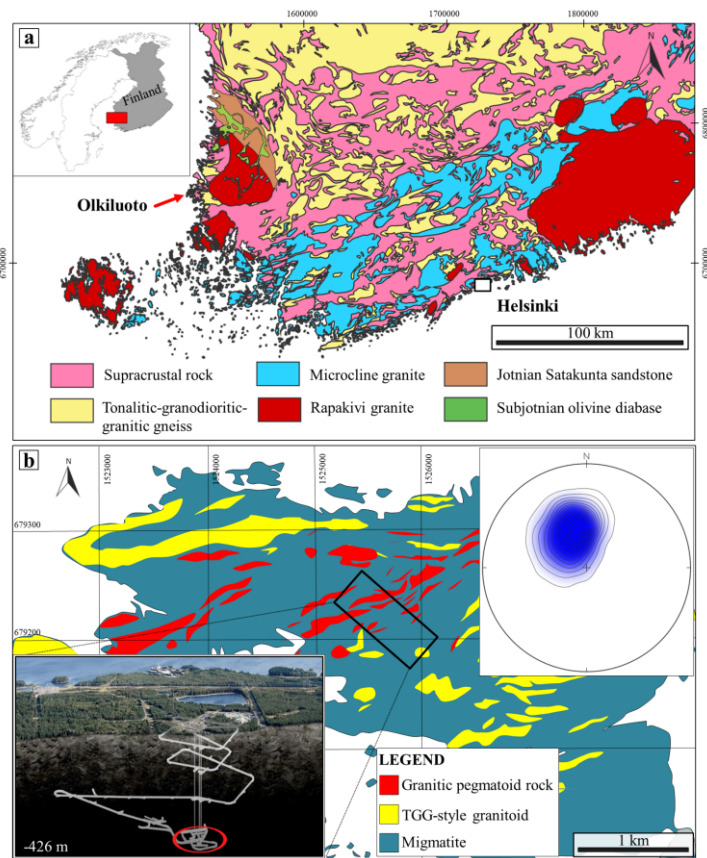
- 1070 Rosso, K. M. and Bodnar, R. J.: Microthermometric and Raman spectroscopic detection limits of CO<sub>2</sub> in fluid inclusions  
1071 and the Raman spectroscopic characterization of CO<sub>2</sub>, *Geochim. Cosmochim. Acta*, 59(19), 3961–3975,  
1072 doi:10.1016/0016-7037(95)94441-H, 1995.
- 1073 [Scheffer, C., Tarantola, A., Vanderhaeghe, O., Rigaudier, T. and Photiades, A.: CO<sub>2</sub> flow during orogenic gravitational  
1074 collapse: Syntectonic decarbonation and fluid mixing at the ductile-brittle transition, \*Chem. Geol.\*, 450, 248–263,  
1075 doi:10.1016/j.chemgeo.2016.12.005, 2017a.](#)
- 1076 [Scheffer, C., Tarantola, A., Vanderhaeghe, O., Voudouris, P., Rigaudier, T., Photiades, A., Morin, D. and Alloucherie, A.:  
1077 The Lavrion Pb-Zn-Fe-Cu-Ag detachment-related district \( Attica , Greece \): Structural control on hydrothermal flow and  
1078 element transfer-deposition, \*Tectonophysics\*, 717, 607–627, doi:10.1016/j.tecto.2017.06.029, 2017b.](#)
- 1079 [Selverstone, J., Axen, G. J., Bartley, J. M.: Fluid inclusion constraints on the kinematics of footwall uplift beneath the  
1080 Brebber Line normal fault, eastern Alps, \*Tectonics\*, 14\(2\), 264-278, 1995.](#)
- 1081 [Selverstone, J., Franz, G., Thomas, S. and Getty, S.: Fluid variability in 2 GPa eclogites as an indicator of fluid behavior  
1082 during subduction, \*Contrib to Mineral and Petrol.\*, 112\(2-3\), 341-357, 1992.](#)
- 1083 Shimizu, M. and Shikazono, N.: [Iron and zinc partitioning between coexisting stannite and sphalerite: a possible indicator  
1084 of temperature and sulfur fugacity](#), *Miner. Depos.*, 20, 314–320, 1985.
- 1085 Scholz, C. H.: *The Mechanics of Earthquakes and Faulting*, Cambridge: Cambridge University Press, 1990.
- 1086 [Sibson, R. H.: A note on fault reactivation, \*J. Struct. Geol.\*, 7\(6\), 751–754, doi:10.1016/0191-8141\(85\)90150-6, 1985.](#)
- 1087 Sibson, R. H.: Earthquake faulting as a structural process, *J. Struct. Geol.*, 11(1–2), 1–14, doi:10.1016/0191-  
1088 8141(89)90032-1, 1989.
- 1089 Sibson, R. H.: Fault-valve behavior and the hydrostatic-lithostatic fluid pressure interface, *Earth Sci. Rev.*, 32(1–2), 141–  
1090 144, doi:10.1016/0012-8252(92)90019-P, 1992a.
- 1091 Sibson, R. H.: Implications of fault-valve behaviour for rupture nucleation and recurrence., *Tectonophysics*, 211(1–4),  
1092 283–293., 1992b.
- 1093 Sibson, R. H.: Load-strengthening versus load-weakening faulting, *J. Struct. Geol.*, 15(2), 123–128, doi:10.1016/0191-  
1094 8141(93)90090-W, 1993.
- 1095 Sibson, R. H.: Structural permeability of fluid-driven fault-fracture meshes, *J. Struct. Geol.*, 18(8), 1996.
- 1096 Sibson, R. H., Robert, F. and Poulsen, K. H.: High-angle reverse faults, fluid-pressure cycling, and mesothermal gold-  
1097 quartz deposits, *Geology*, 16(June 1988), 551–555, doi:10.1130/0091-7613(1988)016<0551:HARFFP>2.3.CO;2, 1988.
- 1098 [Siebenaller, L., Boiron, M. C., Vanderhaeghe, O., Hibsich, C., Jessell, M. W., Andre-Mayer, A. S., France-Lanord, C. and  
1099 Photiades, A.: Fluid record of rock exhumation across the brittle-ductile transition during formation of a Metamorphic Core  
1100 Complex \(Naxos Island, Cyclades, Greece\), \*J. Metamorph. Geol.\*, 31\(3\), 313–338, doi:10.1111/jmg.12023, 2013.](#)
- 1101 Siebenaller, L., Vanderhaeghe, O., Jessell, M., Boiron, M. C. and Hibsich, C.: Syntectonic fluids redistribution and

- 1102 circulation coupled to quartz recrystallization in the ductile crust (Naxos Island, Cyclades, Greece), *J. Geodyn.*, 101, 129–  
1103 141, doi:10.1016/j.jog.2016.07.001, 2016.
- 1104 Skyttä, P. and Torvela, T.: Brittle reactivation of ductile precursor structures: The role of incomplete structural transposition  
1105 at a nuclear waste disposal site, Olkiluoto, Finland, *J. Struct. Geol.*, 0–1, doi:10.1016/j.jsg.2018.06.009, 2018.
- 1106 Spruzeniece, L. and Piazzolo, S.: Strain localization in brittle-ductile shear zones: Fluid-abundant vs. fluid-limited  
1107 conditions (an example from Wyangala area, Australia), *Solid Earth*, 6(3), 881–901, doi:10.5194/se-6-881-2015, 2015.
- 1108 Steele-MacInnis, M., Lecumberri-Sanchez, P. and Bodnar, R. J.: HokieFlincs\_H2O-NaCl: A Microsoft Excel spreadsheet  
1109 for interpreting microthermometric data from fluid inclusions based on the PVTX properties of H2O-NaCl, *Comput.*  
1110 *Geosci.*, 49, 334–337, doi:10.1016/j.cageo.2012.01.022, 2012.
- 1111 Sterner, S. M. and Bodnar J.: Synthetic fluid inclusions - VII. Re-equilibration of fluid inclusions in quartz during  
1112 laboratory-simulated metamorphic burial and uplift, *J. Metamorph. Geol.*, 7, 243–260, 1989.
- 1113 Suominen, V.: The chronostratigraphy of southern Finland, with special reference to Postjotnian and Subjotnian diabases.  
1114 *Bull. Geol. Surv. Finl.*, 356, 100, 1991.
- 1115 Tarantola, A., Diamond, L. W. and Stünitz, H.: Modification of fluid inclusions in quartz by deviatoric stress I:  
1116 Experimentally induced changes in inclusion shapes and microstructures, *Contrib. to Mineral. Petrol.*, 160, 825–843,  
1117 doi:10.1007/s00410-010-0509-z, 2010.
- 1118 Tchalenko, J. S.: Similarities between Shear Zones of Different Magnitudes, *Geol. Soc. Am. Bull.*, 81(6), 1625–1640,  
1119 doi:10.1130/0016-7606(1970)81[1625:SBSZOD]2.0.CO;2, 1970.
- 1120 Tenthorey, E. and Cox, S. F.: Cohesive strengthening of fault zones during the interseismic period: An experimental study,  
1121 *J. Geophys. Res. Solid Earth*, 111(9), 1–14, doi:10.1029/2005JB004122, 2006.
- 1122 Trepmann, C. A. and Stöckhert, B.: Quartz microstructures developed during non-steady state plastic flow at rapidly  
1123 decaying stress and strain rate, *J. Struct. Geol.*, 25(12), 2035–2051, doi:10.1016/S0191-8141(03)00073-7, 2003.
- 1124 Trepmann, C. A. and Stöckhert, B.: Short-wavelength undulatory extinction in quartz recording coseismic deformation in  
1125 the middle crust – An experimental study, *Solid Earth*, 4(2), 263–276, doi:10.5194/se-4-263-2013, 2013.
- 1126 Trepmann, C. A., Stöckhert, B., Dorner, D., Moghadam, R. H., Küster, M. and Röller, K.: Simulating coseismic  
1127 deformation of quartz in the middle crust and fabric evolution during postseismic stress relaxation - An experimental study,  
1128 *Tectonophysics*, 442(1–4), 83–104, doi:10.1016/j.tecto.2007.05.005, 2007.
- 1129 Trepmann, C. A., Hsu, C., Hentschel, F., Döhler, K., Schneider, C. and Wichmann, V.: Recrystallization of quartz after  
1130 low-temperature plasticity – The record of stress relaxation below the seismogenic zone, *J. Struct. Geol.*, 95, 77–92,  
1131 doi:10.1016/j.jsg.2016.12.004, 2017.
- 1132 Van den Kerkhof, A., Kronz, A. and Simon, K.: Deciphering fluid inclusions in high-grade rocks, *Geosci. Front.*, 5(5),  
1133 683–695, doi:10.1016/j.gsf.2014.03.005, 2014.
- 1134 [Van Noten, K., Muechez, P. and Sintubin, M.: Stress-state evolution of the brittle upper crust during compressional tectonic](#)

- 1135 [inversion as defined by successive quartz vein types \( High-Ardenne slate belt , Germany \). J. Geol. Soc. London,](#)  
1136 [168\(2004\), 407–422, doi:10.1144/0016-76492010-112.Stress-state, 2011.](#)
- 1137 Viola, G., Mancktelow, N. S. and Miller, J. A.: Cyclic frictional-viscous slip oscillations along the base of an advancing  
1138 nappe complex: Insights into brittle-ductile nappe emplacement mechanisms from the Naukluft Nappe Complex, central  
1139 Namibia, *Tectonics*, 25(3), 1–20, doi:10.1029/2005TC001939, 2006.
- 1140 Viola, G., Venvik Ganerød, G. and Wahlgren, C. H.: Unraveling 1.5 Ga of brittle deformation history in the Laxemar-  
1141 Simpevarp area, southeast Sweden: A contribution to the Swedish site investigation study for the disposal of highly  
1142 radioactive nuclear waste, *Tectonics*, 28(5), 1–29, doi:10.1029/2009TC002461, 2009.
- 1143 Viola, G., Mattila, J., Zwingmann, H., Todd, A. and Raven, M.: Structural and K / Ar Illite Geochronological Constraints  
1144 on the Brittle Deformation History of the Olkiluoto Region, Southwest Finland, Posiva Working Report 2011, Posiva Oy,  
1145 Eurajoki, 2011.
- 1146 Viola, G., Scheiber, T., Fredin, O., Zwingmann, H., Margreth, A. and Knies, J.: Deconvoluting complex structural histories  
1147 archived in brittle fault zones, *Nat. Commun.*, 7, 1–10, doi:10.1038/ncomms13448, 2016.
- 1148 Vityk, M. O. and Bodnar, R. J.: Textural evolution of synthetic fluid inclusions in quartz during reequilibration, with  
1149 applications to tectonic reconstruction, *Contrib. to Mineral. Petrol.*, 121(3), 309–323, doi:10.1007/BF02688246, 1995.
- 1150 Vityk, M. O. and Bodnar, R. J.: Statistical microthermometry of synthetic fluid inclusions in quartz during decompression  
1151 reequilibration, *Contrib. to Mineral. Petrol.*, 132(2), 149–162, doi:10.1007/s004100050413, 1998.
- 1152 Vityk, M. O., Bodnar, R. J. and Schmidt, C. S.: Fluid inclusion as a tectonothermobarometers: Relation between pressure-  
1153 temperature history and reequilibration morphology during crystal thickening, *Geology*, 22, 731–734, doi:10.1130/0091-  
1154 7613(1994)022<0731:FIATRB>2.3.CO, 1994.
- 1155 Wehrens, P., Berger, A., Peters, M., Spillmann, T. and Herwegh, M.: Deformation at the frictional-viscous transition:  
1156 Evidence for cycles of fluid-assisted embrittlement and ductile deformation in the granitoid crust, *Tectonophysics*, 693,  
1157 66–84, doi:10.1016/j.tecto.2016.10.022, 2016.
- 1158 Wilkins, R. W. T. and Barkas, J. P.: Fluid inclusions, Deformation and Recrystallization in Granite Tectonites, *Contrib.*  
1159 *Mineral. Petrol.*, 65, 293-299, 1978.

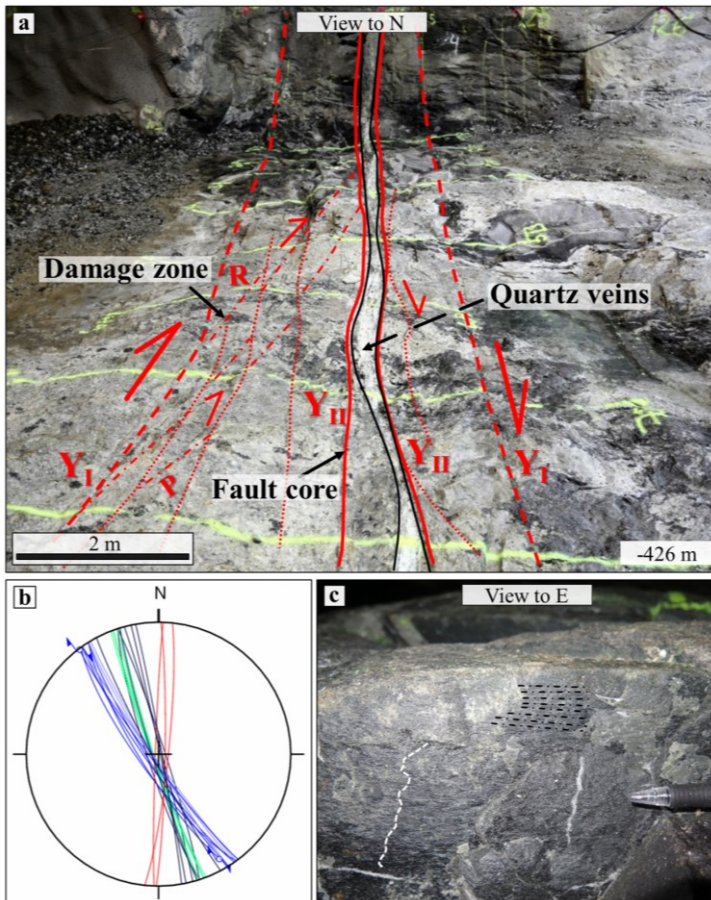
1160

1161



1162  
 1163  
 1164  
 1165  
 1166  
 1167

Figure 1. (a) Simplified geological map of southwestern Finland modified after Mattila and Viola (2014). (b) Geological sketch of the Olkiluoto Island. The upper right inset shows the poles to foliation planes measured from all available Olkiluoto drill cores ( $N = 4479$ , equal area, lower hemisphere projection; Mattila and Viola, 2014). The lower left inset is a panoramic photograph with an overlay drawing of the underground infrastructure (photo courtesy of Posiva Oy, Finland). The red circle shows the depth location of BFZ300. Coordinates are given in the local KKK1 coordinate system.



1168

1169

1170

1171

1172

1173

1174

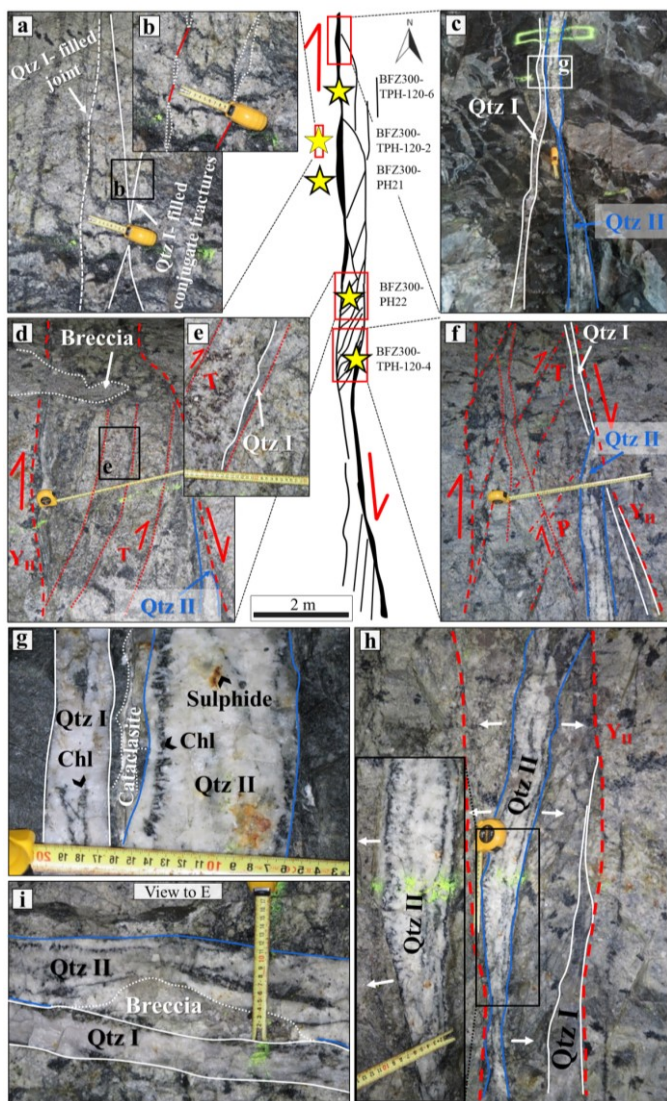
1175

1176

Figure 2. (a) View to the north and interpretation of the structural elements of the fault, whose core hosts BFZ300 two generations of quartz-chlorite veins (thicker black lines). (b) Lower-hemisphere, equiangular projection of conjugate fault segments (blue great circles; lines are used for dextral faults; white great circles; lines indicate sinistral faults), cleavage (green great circles) and quartz-chlorite veins infilling joints are presented with green and black coloured lines respectively (black great circles). (c) Slickensides (white dashed line) and slickenlines (black dashed lines) on a chlorite-decorated, -NW-SE striking fracture plane at the vein-host rock boundary interface - and the geometry of the R- and P- shears suggest indicating dextral strike-slip kinematics. Slickensides and slickenlines are observed at the vein-host rock boundary. Sample location is reported in panel a with a white square.

1177  
1178

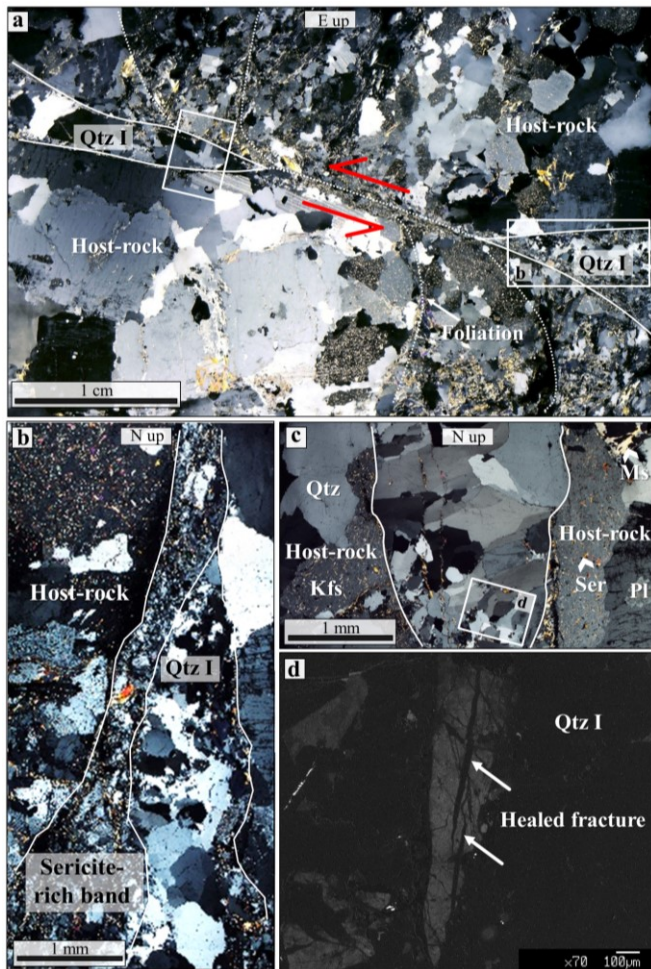






1180 Figure 3. BFZ300 fault geometry and architecture (centre of figure) with examples of representative structural outcrop features. The red  
1181 rectangles locate the areas along the fault segments where detailed outcrop photos were taken. Stars locate hand and drill core samples. Stars  
1182 with a black layout outline identify samples used for the microthermometric study. Note that the fault is made of two main segments offset  
1183 laterally at a sinistral compressive step-over zone with overall dextral kinematics. Fault core quartz veins are shown by thicker black lines in the  
1184 schematic model (centre of figure), while blue and white lines highlight the positions of the two types of quartz veins in the outcrop pictures. (a)  
1185 Damage zone made of mm-thick, en-echelon veins connected by conjugate shear segments. (b) Detail of (a) showing fractures filled by the first  
1186 quartz generation (Qtz I). (c) Two distinct generations of quartz-chlorite veins recognised in the fault core (Qtz I and Qtz II). (d) Detail of the  
1187 sinistral compressional step-over zone characterized by multiple and parallel T fractures, filled by Qtz I. A brecciated body is crosscut by the Y  
1188 planes. (e) Detail of a tensional fracture infilled by Qtz I. (f) Compressional structures (P shears) from the step-over zone and relationships  
1189 between Qtz I and Qtz II within the fault. The Riedel geometry suggests that the Qtz II vein formed due to the reactivation of the internal  
1190 principal slip zones (Y<sub>1</sub>). Note the Qtz II vein cutting the Qtz I vein. (g) Juxtaposed Qtz I and Qtz II veins. Qtz I veins are thinner and  
1191 made of a translucent, small grained quartz. In contrast, Qtz II veins, which contain pockets of sulphide aggregates, are thicker and made of larger  
1192 and euhedral quartz. Chlorite occurs as minor phase in both vein types of veins, but only in Qtz II veins it forms long and prismatic aggregates  
1193 growing perpendicular to the fracture walls. In Qtz I veins, chlorite is small grained and forms thin levels within the quartz. Notice the presence  
1194 of a cataclastic band between the two veins. (h) Spatial continuity of the chlorite aggregates within the Qtz II veins, which grow always orthogonal  
1195 to the vein boundaries. The inset shows the detail of the prismatic aggregates forming long and parallel ribbons. This open space filling texture  
1196 suggests hybrid conditions of reactivation of the older Qtz I veins. (i) Small quartz breccia formed between the two generations of quartz veins.  
1197

Formattato: Colore carattere: Rosso, Pedice



1198

1199

1200

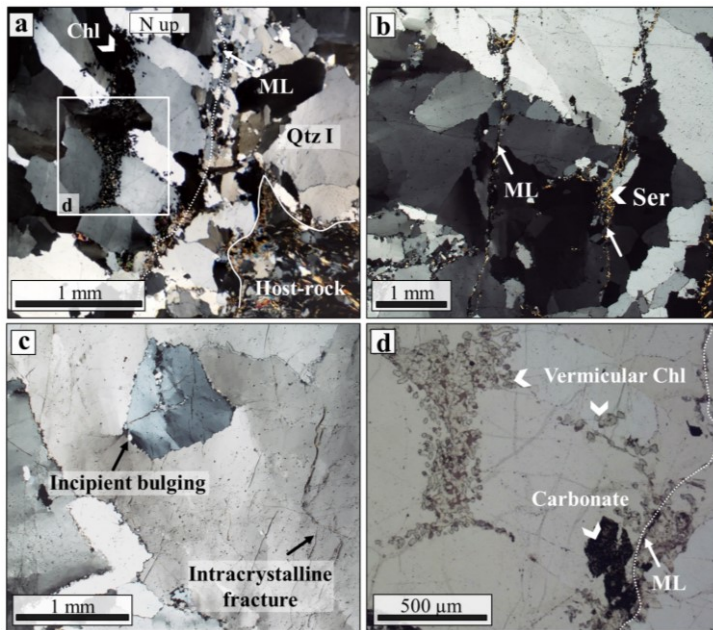
1201

1202

1203

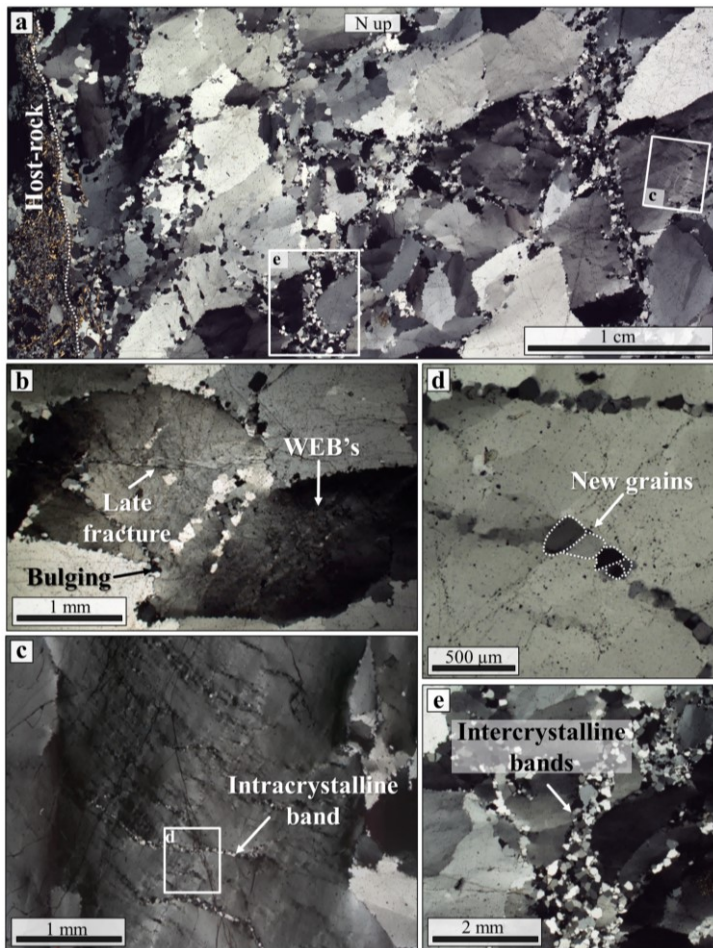
Figure 4. Microtextural characteristics of Qtz I from the damage zone of BFZ300 (sample: TPH-120-2). (a) ~~Composition of~~ Stitched photomicrographs of a Qtz I vein interconnecting with a sinistral shear band (crossed nicols). Faulting kinematics is suggested by drag folds in the host rock. (b) Tip of Qtz I vein hosted by a sericite-rich cataclastic band of the host rock. (c) Detail of panel a showing open-space filling texture in the Qtz I vein. Notice the sericite microfractures crosscutting Qtz I. (d) Panchromatic cathodoluminescence image of Qtz I showing healed microfractures crosscutting the crystal.

1204  
1205



1206

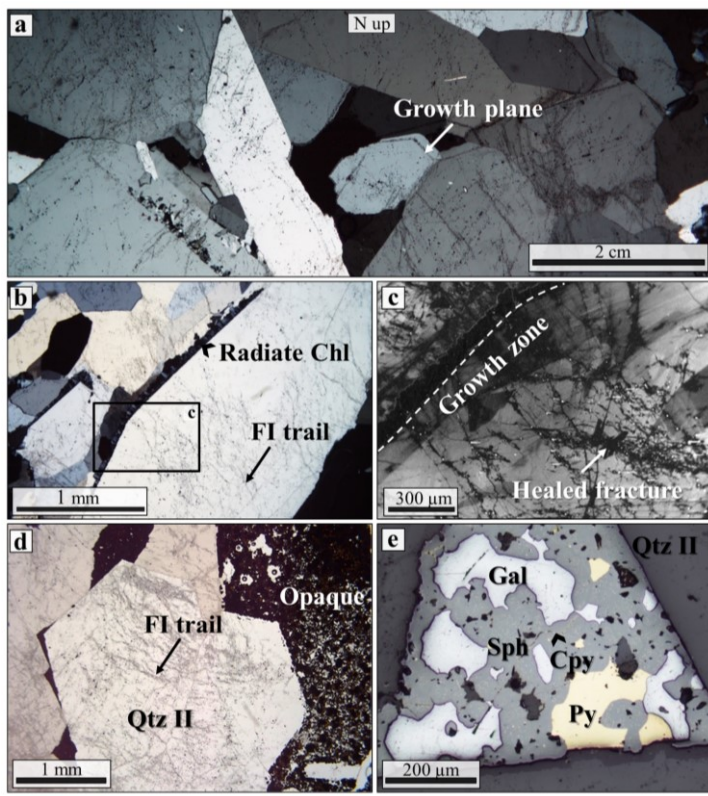
1207 Figure 5. Microtextural characteristics of Qtz I from the damage zone of BFZ300 (samples PH21 and TPH-1202). (a) Stacked microphotographs  
1208 of a Qtz I vein showing elongate-blocky texture with crystals growing obliquely with respect to the vein boundaries, which suggests growth  
1209 under oblique dilatation. A series of median lines (ML) are marked by (b) sericite crystals suggesting repeated crack-and-seal. Quartz crystals  
1210 show low temperature plasticity-crystal-plastic deformation by undulose extinction and extinction bands. (c) Detail of plastic deformation in  
1211 damage zone quartz veins: distorted crystals showing incipient bulging, recrystallization and intracrystalline granular fracturing. (d) Detail (plane  
1212 polarized light) of the median line ML and secondary fractures both decorated by vermicular chlorite and aggregates of REE-bearing carbonate.  
1213



1214  
 1215  
 1216  
 1217  
 1218  
 1219  
 1220

Figure 6. Microtextural characteristics of Qtz I from the BFZ300 core (sample TPH-120-4). (a) Stacked photomicrographs showing the typical heterogeneous grain size of Qtz I (30-800  $\mu\text{m}$ ). (b) Evidence of plastic deformation of Qtz I from the fault core given by bulging of the largest crystals, wide extinction bands and undulose extinction. Note the late brittle fractures crosscutting all the previously formed plastic features. (c) Intracrystalline deformation bands within a large crystal. (d) Detail of (c) showing the typical grain size of the band (50-250  $\mu\text{m}$ ). Intracrystalline deformation bands are oriented at  $<30^\circ$  with respect to the BFZ300 vein walls and can be up to 2 mm in length. (e) Intercrystalline deformation band showing a thickening at the triple junction of larger grains. These intercrystalline bands are parallel to the strike of BFZ300.





1221

1222

1223

1224

1225

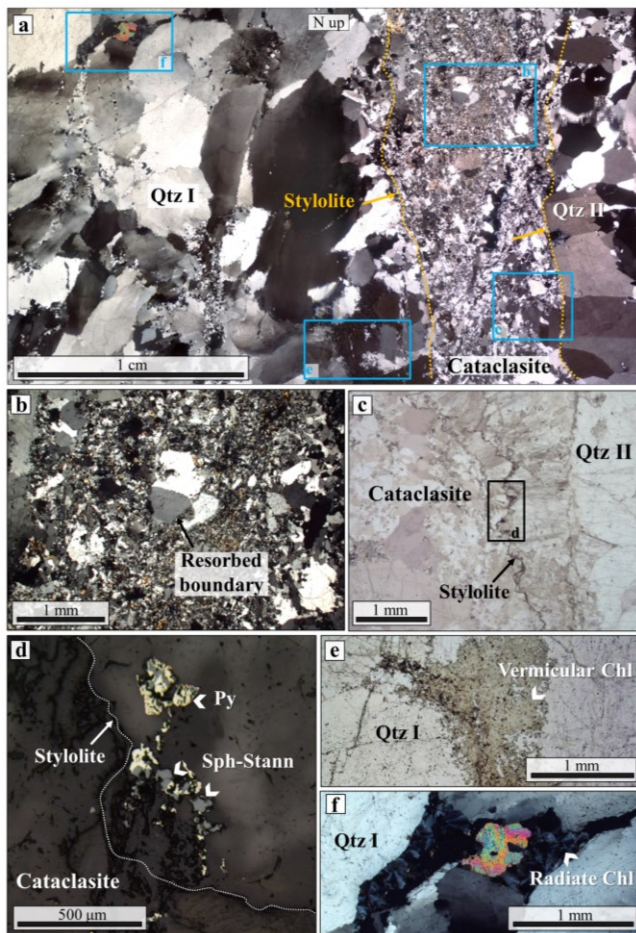
1226

1227

1228

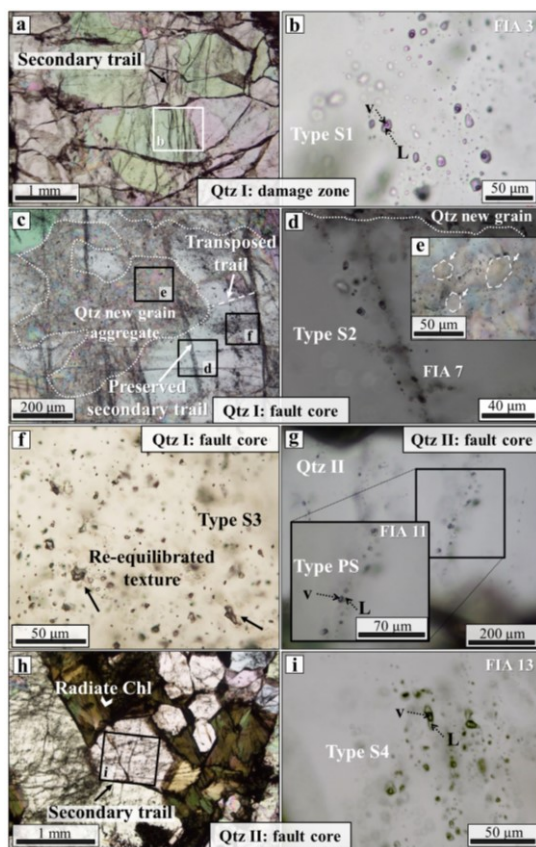
1229

Figure 7. Microstructural characteristics of Qtz II from BFZ300 (samples TPH-120-6, PH22). (a) Stretched photomicrographs of Qtz II vein from the fault core. Notice the coarse quartz crystals and their elongated-blocky texture. Primary growth textures are sometimes visible and are marked by solid inclusions and decrepitated FIAs. (b) Radiate chlorite crystals along a prismatic Qtz II crystal boundary. Note that Qtz II is crosscut by numerous trails of FIAs. (c) Panchromatic cathodoluminescence image of the same large Qtz II crystal from panel b, showing radiate chlorite along the crystal boundary and a primary growth zone cut by a set of healed fractures. (d) Euhedral quartz crystals set within opaque phases and crosscut by a network of thin microfractures. (e) Reflected light photomicrograph showing the opaque mineral assemblage typically associated with Qtz II, i.e. subhedral to anhedral sphalerite, pyrite, and galena. Chalcopyrite is a minor phase and occurs as small round inclusions within sphalerite (chalcopyrite "disease") or as large subhedral/anhedral masses together with galena.



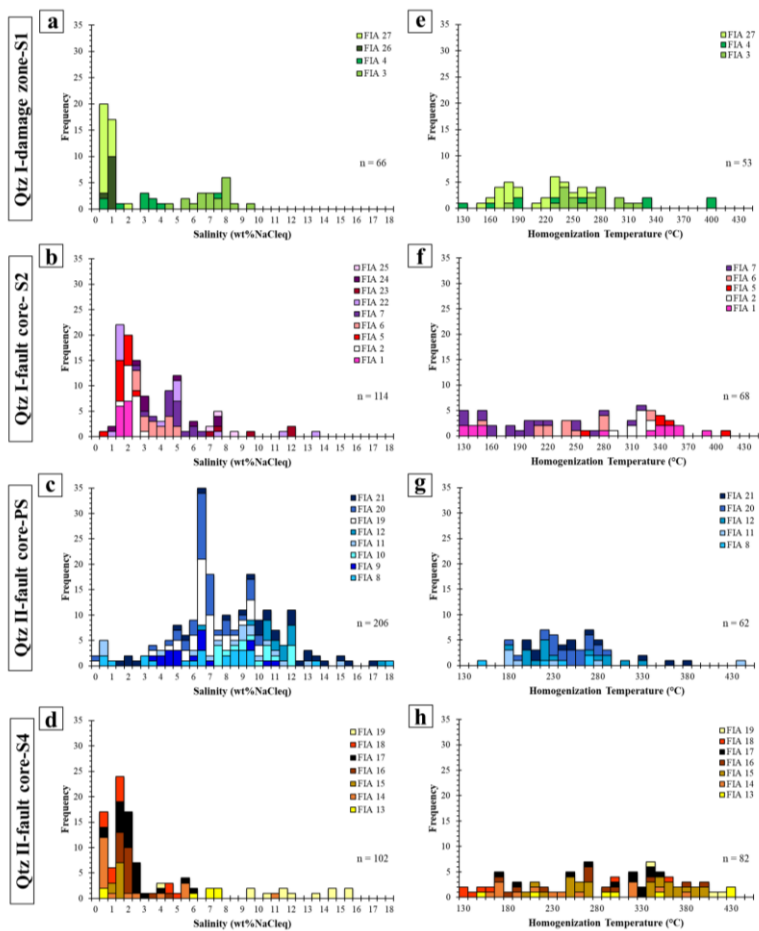
1230

1231 Figure 8. **Microstructures** of the cataclasite juxtaposing Qtz I and Qtz II veins (sample TPH-120-4). (a) Stretched photomicrographs covering the  
 1232 contact between the two quartz veins and the intervening 5 mm-thick cataclastic band. (b) Cataclastic band **constituted by containing** large Qtz I  
 1233 fragments (8-12 mm) embedded within a finer matrix (20-200  $\mu\text{m}$  in size) of sericite and **recrystallized** quartz. The largest crystals show lobate  
 1234 boundaries, suggesting dissolution and local resorption along the clast-matrix interface. (c) Stylolite seams **at the boundary of the cataclasite** that  
 1235 strike parallel to the BFZ300. (d) Reflected-light photomicrograph showing anhydrous pyrite, chalcopyrite, stannite, and sphalerite  
 1236 arranged along the stylolite as residual products of pressure solution. (e) Vermicular **and radiate (f) chlorite aggregates** associated with Qtz I  
 1237 close to the cataclastic band.



1239  
1240  
1241  
1242  
1243  
1244  
1245  
1246  
1247  
1248  
1249

Figure 9. Characteristics textures of FIAs hosted within the BFZ300 quartz (samples PH21, TPH-120-4, TPH-120-6). (a) Secondary trails crosscutting large Qtz I crystals of the damage zone. (b) Detail of (a) showing the phase ratios of one of the studied secondary assemblages (FIA3), most representative of Type S1 FIA. (c) Long secondary transgranular trails crosscutting Qtz I of the fault core, dismembered by intercrystalline fractures, infilled by quartz new grains. Qtz I fault core also hosts set of short sub-trails developed at high angle with respect to the long trails. (d) Detail of Type S2 FIA entrapped along a preserved secondary fracture trail. (e) Small inclusions (<1μm) arranged along the boundaries of new polygonal quartz. (f) Example of Type S3 FIA arranged as isolated clusters inside ductile deformed fault core Qtz I. These trails formed during a brittle deformation stage that pre-dates ductile re-crystallization. (g) Pseudosecondary FIA associated with Qtz II-chlorite (FIA11). [Enlarge](#)—The enlargement shows the phase ratio details. (h) Small scale view of secondary FIAs crosscutting Qtz II. (i) Detail of secondary trails crosscutting euhedral Qtz II (FIA 13). In all photographs north points up.

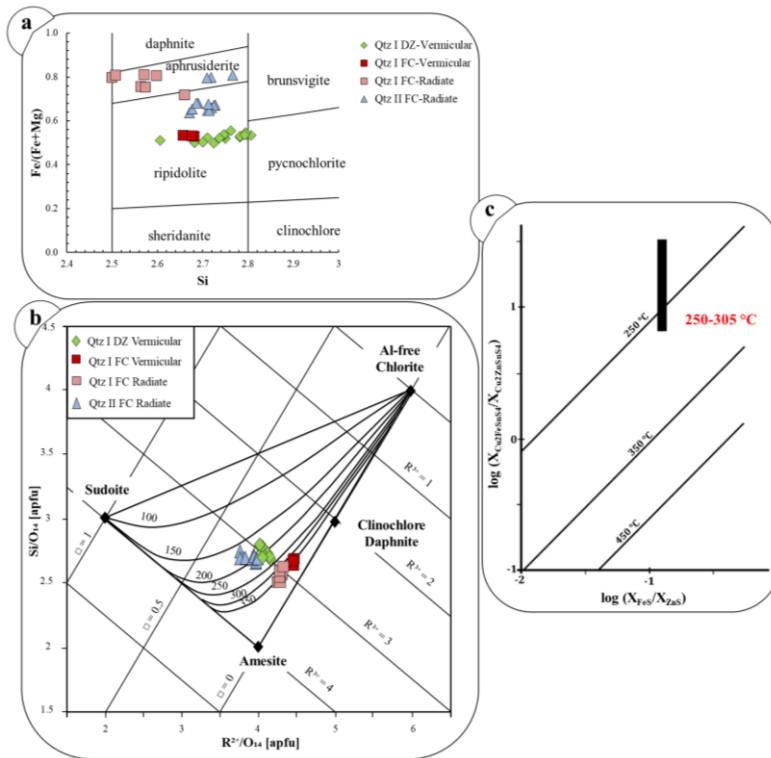


1250  
 1251  
 1252  
 1253  
 1254  
 1255  
 1256  
 1257

Figure 10. Microthermometric data of the studied FIAs. Panels a-d show the bulk salinities of individual FIAs calculated from the  $T_{mice}$  data, while panels e-h refer to the temperatures of final homogenization of the same assemblages. Notice that the data report the properties of individual FIAs according to their occurrence within Qtz I of the damage zone, Qtz I from the fault core, and Qtz II from the fault core. Notice that pseudosecondary (PS) and secondary (S) FIAs identify progressive later stages of fluid entrapment, and can be used to constrain the fluid properties in the fault zone. Notice also that the measured ranges of  $T_{thot}$  spread across  $T$  intervals that are too large to represent entrapment at equilibrium (e.g., FIA7 of Qtz I from fault core: 130-320 °C), which suggests post-entrapment re-equilibration of the inclusions. Fluid bulk composition is expressed as salinity, which is conventionally reported as weight percent of NaCl equivalents (wt%NaCleq, Roedder,1984).



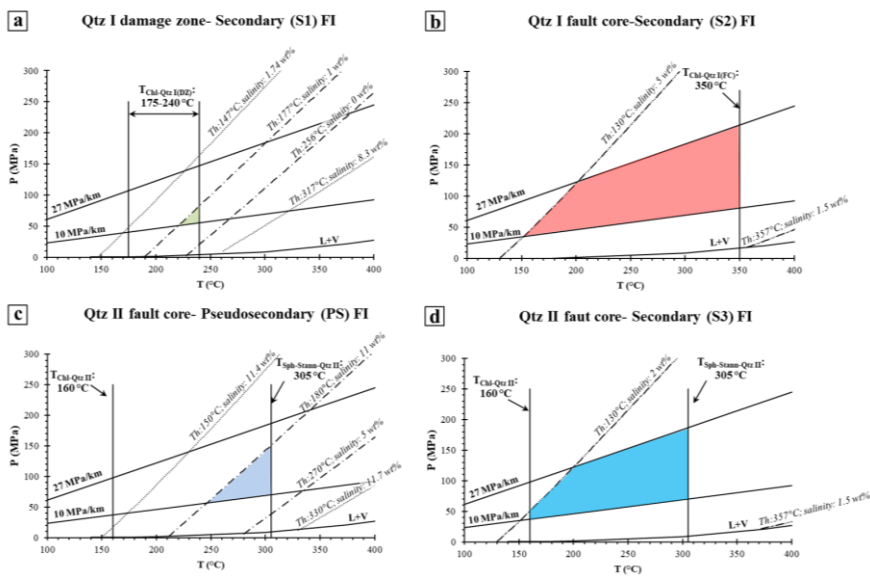
1258  
1259



1260

1261  
1262  
1263  
1264  
1265  
1266  
1267  
1268  
1269  
1270  
1271

Figure 11. Chlorite chemical composition diagram and mineral-pair geothermometry applied to the assemblages of the Qtz I- and Qtz II veins. (a) Chlorite compositional diagram based on Hey (1954). The classification diagram shows a wide compositional range for chlorite across the BFZ300. Green, red, pink and light blue symbols indicate distinct chlorite textures in association with Qtz I and Qtz II veins. (b) Chlorite-quartz formation temperature estimated using the method of Bourdelle and Cathelineau (2015). Green, red, and light blue symbols indicate the distinct textural types of chlorite in Qtz I and II, respectively. The maximum temperature is from the Qtz I-chlorite pair from the fault core. The other groups of chlorites in the 150-250 °C range, indicate a second stage of quartz-chlorite precipitation in the fault core and damage zone, in line with microthermometric constraints. (c) Estimated temperature of formation of sphalerite-stannite in association with Qtz II vein (based on formation estimate we used the method of Shimizu & Shikazono (1985), that uses Fe and Zn partitioning between stannite and sphalerite. The region of the plot that was calibrated with this geothermometer lies between the 250 and 450 °C isotherms. Hence, compositions corresponding to T < 250 °C should be interpreted with caution.



1272

1273

1274

1275

1276

1277

1278

1279

1280

1281

1282

1283

1284

1285

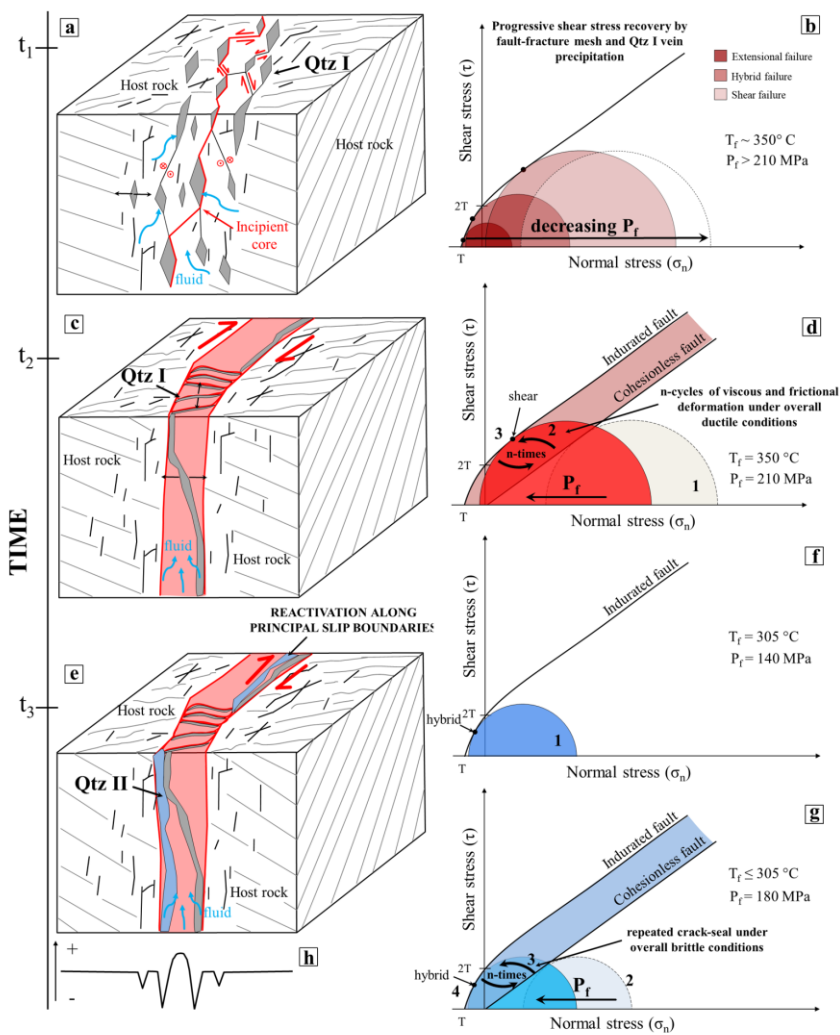
1286

1287

1288

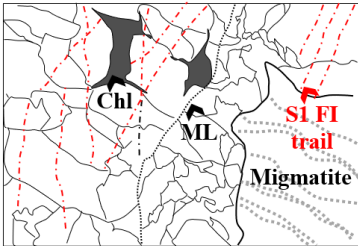
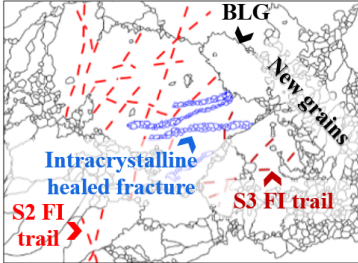
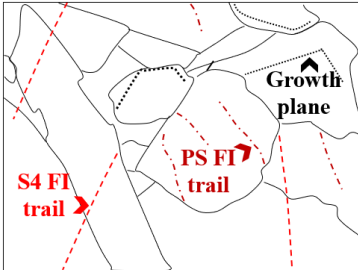
1289

Figure 12. P-T diagrams showing the ranges of PT trapping conditions of the analysed fluid inclusions. P-T ranges have been estimated from petrographically discriminated petrographically and on the basis of identified in each structural domains. Fluid pressures are related to (a) secondary inclusions in Qtz I from the fault damage zone; Qtz I; (b) secondary inclusions from Qtz I in the fault core-Qtz I; (c-d) pseudosecondary inclusions trapped in Qtz II in the fault core and (d) secondary inclusions in the Qtz II-Qtz II. Thin dashed lines indicate maximum and minimum isochores of FIAs in each structural domain. The light coloured areas are defined by the uppermost and lowermost sets of fluid inclusion isochores, while the dark coloured areas identify the probable PT trapping ranges defined by: i) the slope and position of the fluid inclusion isochores as determined by the most representative salinity and homogenization temperature range (Supplementary Material for details); ii) related to the pressure range calculated for isochores computed for the most probable composition of the pristine fluid (salinity between 0 and 5 wt% NaCl<sub>eq</sub>, see text for more details); iii) The pressure-temperature areas are also defined by the mineral pairs geothermometry and iii) hydrostatic and lithostatic pore-fluid pressures computed assuming a regional geothermal gradient of c. 43 °C/km (assuming retrograde conditions of P c. 4 kbar and T c. 650 °C, from Kärki and Paulamäki, 2006). The L<sub>1</sub> (dotted vertical lines), and by the liquid-vapour equilibrium curves for the H<sub>2</sub>O-NaCl modeled fluid is also indicated. The 240 °C vertical line represents the equilibrium temperature between chlorite and damage zone Qtz I. The 350 °C vertical line is the equilibrium temperature between chlorite and fault core Qtz I. The 250-305 °C vertical lines mark the lowest and highest sphalerite-stannite equilibrium temperature with Qtz II in the BFZ300 fault core. The thick lower curve marks the bundle of liquid-vapour curves for a 1.5 wt% NaCl fault fluid.



1291 Figure 13. Conceptual model of the temporal and mechanical evolution of the BFZ300 fault zone (see text for more details). Grey lines: traces  
1292 of metamorphic foliation. Black lines: fractures related to the BFZ300 structural development. (a) Initial embrittlement of the migmatitic  
1293 basement occurred by fracture coalescence (red line) under (b) initial lower differential stress conditions and high fluid pressure and followed  
1294 by a transient increase of differential stress. A first generation of quartz veins (Qtz I) precipitated inside the diffuse network of joints and  
1295 hybrid/shear fractures which formed during this first deformation stage. (c) Progressive strain localization and fluid channeling within the fault  
1296 core occurred by (d) episodically renewed fluid-pressure build-up driven by cycles of brittle and ductile deformation. (e-g) Progressive  
1297 exhumation and cooling of the fault system occurred concomitant with several brittle reactivation episodes of the fault zone under hybrid  
1298 conditions and fluid pressure lower than during the previous deformational stages. Lastly, a second generation of quartz veins (Qtz II) was  
1299 emplaced, mainly along the principal slip boundaries of the fault core, following the Qtz I vein as shown by (h) the strenght profile across the  
1300 fault architecture, that suggests lower tensile strength values (and hence higher reactivation potential) along the Qtz I vein / host rock walls.

1301 Table 1: Schematic summary of main microstructures, fluid properties, and PT deformation conditions in the quartz veins of the BFZ300 fault.

<i>Structural zone and sample</i>	<i>Qtz type</i>	<i>Deformation type</i>	<i>Microstructures</i>	<i>Microthermometric properties</i>	<i>Fluid pressure (<math>P_f</math>) and mineral pair thermometry</i>
Damage zone (PH-21)	Qtz I	Brittle/Ductile		$T_{\text{mice}}$ S1: -0.1 to -5.9 °C $T_{\text{htot}}$ S1: 150-400 °C	$T_{\text{Chl-QtzI (DZ)}}$ : 175-240 °C $P_f$ (S1): 50-80 MPa
Fault core (TPH120-4A)	Qtz I	Cyclic Brittle/Ductile		$T_{\text{mice}}$ S2: -0.4 to -8.2 °C $T_{\text{htot}}$ S2: 130-410 °C	$T_{\text{Chl-QtzI (FC)}}$ : 350 °C $P_f$ (S2) 30-210 MPa
Fault core (TPH120-6) (TPH120-4)	Qtz II	Brittle		$T_{\text{mice}}$ PS: -0.1 to -13.6 °C $T_{\text{htot}}$ PS: 150-440 °C $T_{\text{mice}}$ S4: 0 to -11 °C $T_{\text{htot}}$ S4: 130-430 °C	$T_{\text{Chl-QtzII}}$ : 160-220 °C $T_{\text{Sph-Stann-Qtz II}}$ : 250-305 °C $P_f$ (PS): 50-140 MPa $P_f$ (S4): 40-180 MPa

1302 Note: microstructures are coupled with the corresponding FI types and PT constraints derived from the collected dataset. See text for more explanations.  
 1303  
 1304 Notice that we combine structural and geochemical data to constrain the relationships between stages of mineral-scale deformation and fluid circulation,  
 1305 which in turn defines the relative chronology of stages of fluid flow during faulting.  
 1306 ML: median line; Blg: bulging.

1307  
 1308  
 1309  
 1310  
 1311  
 1312

1313 Table 2: Chlorite EPMA from various structural zones of BFZ300

Sample	4A	4A	4A	4A	4A	4A	PH21	PH21	PH21	2	2	2	6	6	6	6
Structural zone	FC	FC	FC	FC	FC	FC	DZ	DZ	DZ	DZ	DZ	DZ	FC	FC	FC	FC
Quartz type	Qtz I	Qtz I	Qtz I	Qtz I	Qtz I	Qtz I	Qtz I	Qtz I	Qtz I	Qtz I	Qtz I	Qtz I	Qtz II	Qtz II	Qtz II	Qtz II
Textural type	Verm	Verm	Verm	Rad	Rad	Rad	Verm	Verm	Verm	Verm	Verm	Verm	Rad	Rad	Rad	Rad
Na <sub>2</sub> O	0.04	0.07	0.00	0.08	0.08	0.03	0.05	0.02	0.04	0.03	0.01	0.05	0.04	0.06	0.01	0.01
TiO <sub>2</sub>	0.02	0.01	0.00	0.00	0.03	0.01	0.09	0.04	0.01	0.01	0.01	0.03	0.03	0.03	0.04	0.13
MnO	0.59	0.65	0.62	0.53	0.56	0.48	0.24	0.24	0.30	0.48	0.37	0.43	0.64	0.57	0.71	0.60
K <sub>2</sub> O	0.06	0.02	0.04	0.07	0.06	0.04	0.01	0.01	0.03	0.10	0.05	0.07	0.03	0.02	0.05	0.01
MgO	13.66	13.79	13.74	6.61	5.13	6.75	13.95	14.06	13.29	12.85	12.57	12.59	4.85	4.87	8.73	8.05
SiO <sub>2</sub>	25.49	26.00	25.83	23.62	22.89	23.91	27.24	27.02	27.49	27.43	27.88	27.79	25.63	25.64	26.5	26.13
Cr <sub>2</sub> O <sub>3</sub>	0.00	0.01	0.04	0.00	0.00	0.06	0.04	0.03	0.06	0	0.06	0.01	0	0.02	0.01	0
FeO	27.86	27.74	27.87	36.61	38.49	36.75	24.68	25.21	26.07	25.97	26.06	25.77	34.26	33.84	30.08	30.47
CaO	0.03	0.04	0.05	0.00	0.06	0.03	0.01	0.02	0	0.05	0.05	0.03	0.01	0.04	0.04	0.02
Al <sub>2</sub> O <sub>3</sub>	22.04	22.13	22.00	22.89	23.35	22.98	24.13	24.75	24.91	24.02	23.48	23.21	24.23	24.64	24.49	25.02
Cl	0.00	0.00	0.01	0.03	0.02	0.04	0.01	0	0	0.01	0	0	0.03	0.02	0.02	0.01
Total	89.78	90.45	90.20	90.44	90.67	91.09	90.69	91.42	92.23	91.12	90.81	90.08	89.82	89.94	90.78	90.48
No. ions in formula																
Based on 28 (O,OH)																
Na	0.02	0.03	0	0.03	0.03	0.01	0.02	0.01	0.01	0.01	0.01	0.02	0.02	0.03	0	0.01
Ti	0	0	0	0	0	0	0.01	0.01	0	0	0.01	0	0.01	0.0	0.01	0.02
Mn	0.10	0.11	0.11	0.10	0.10	0.09	0.04	0.04	0.05	0.08	0.06	0.07	0.12	0.10	0.12	0.11
K	0.01	0	0.01	0.02	0.02	0.01	0	0	0.01	0.02	0.01	0.02	0.01	0	0.01	0
Mg	4.25	4.25	4.25	2.14	1.68	2.17	4.18	4.19	3.93	3.86	3.79	3.82	1.55	1.55	2.69	2.49
Si	5.32	5.37	5.36	5.14	5.02	5.15	5.48	5.40	5.46	5.53	5.64	5.66	5.49	5.47	5.48	5.43
Cr	0	0	0.01	0	0	0.01	0.01	0	0.01	0	0.01	0	0	0	0	0
Fe <sup>2+</sup>	4.86	4.79	4.83	6.66	7.06	6.62	4.15	4.21	4.33	4.38	4.40	4.39	6.14	6.04	5.20	5.29
Ca	0.01	0.01	0.01	0	0.01	0.01	0	0	0	0.01	0.01	0.01	0	0.01	0.01	0
Al	5.42	5.39	5.38	5.86	6.04	5.84	5.72	5.83	5.83	5.71	5.59	5.57	6.12	6.20	5.97	6.13
Cl	0	0	0	0.01	0.01	0.01	0	0	0	0	0	0	0.01	0.01	0.01	0
Fe	4.86	4.79	4.83	6.66	7.06	6.62	4.15	4.21	4.33	4.38	4.40	4.39	6.14	6.04	5.20	5.29
Al Tetr	2.68	2.63	2.64	2.86	2.98	2.85	2.52	2.60	2.54	2.47	2.37	2.34	2.51	2.53	2.52	2.57
Al Oct	2.73	2.76	2.73	3.00	3.06	2.99	3.20	3.22	3.29	3.24	3.23	3.23	3.61	3.67	3.45	3.56
<u>Fe/(Fe+Mg)</u>	<u>0.53</u>	<u>0.53</u>	<u>0.53</u>	<u>0.76</u>	<u>0.81</u>	<u>0.75</u>	<u>0.50</u>	<u>0.50</u>	<u>0.52</u>	<u>0.53</u>	<u>0.54</u>	<u>0.53</u>	<u>0.80</u>	<u>0.79</u>	<u>0.66</u>	<u>0.68</u>
Based on 28 (O,OH)																
R <sup>2+</sup>	9.11	9.04	9.08	8.80	8.74	8.79	8.33	8.40	8.26	8.24	8.19	8.21	7.69	7.59	7.90	7.79
Si	5.32	5.37	5.36	5.14	5.02	5.15	5.48	5.40	5.46	5.53	5.64	5.66	5.49	5.47	5.48	5.43
Based on 14 (O,OH)																
R <sup>2+</sup>	4.55	4.52	4.54	4.40	4.37	4.40	4.17	4.20	4.13	4.12	4.10	4.10	3.84	3.79	3.95	3.89
Si	2.66	2.68	2.68	2.57	2.51	2.58	2.74	2.70	2.73	2.77	2.82	2.83	2.75	2.74	2.74	2.71

1314

1315

1316

1317

1318

1319

1320

1321

1322

1323

1324 Table 3: Representative EPMA of sulphides associated with Qtz II

Analysis	Structural zone	Qtz type	Mineral	S	Fe	Cu	As	Pb	Ni	Zn	Ti	Sn	Total
TPH120-6-14	Core	II	pyrite	55.02	47.50	0.01	0.00	0.00	0.02	0.00	0.00		102.55
TPH120-6-17	Core	II	pyrite	54.08	47.19	0.00	0.01	0.00	0.00	0.00	0.00		101.28
TPH120-6-18	Core	II	sphalerite	34.46	6.46	0.09	0.01	0.00	0.03	59.62	0.02		100.69
TPH120-6-19	Core	II	sphalerite	34.48	6.24	0.08	0.06	0.00	0.04	59.61	0.02		100.53
TPH120-4A-34	Core	II	pyrite	54.49	47.40	0.05	0.00	0.00	0.00	0.00	0.00		101.94
TPH120-4A-35	Core	II	pyrite	54.13	47.26	0.02	0.04	0.00	0.00	0.01	0.55		102.01
TPH120-4A-38	Core	II	galena	13.40	0.00	0.00	0.00	86.63	0.00	0.32	0.01		100.36
TPH120-4A-59	Core	II	galena	13.50	0.06	0.00	0.01	87.04	0.00	0.10	0.01		100.72
TPH120-4A-40	Core*	II	sphalerite	35.06	9.46	0.05	0.00	0.00	0.00	56.74	0.01		101.32
TPH120-4A-43	Core*	II	sphalerite	34.69	9.04	0.01	0.03	0.00	0.00	57.51	0.01		101.28
TPH120-4A-41	Core	II	chalcopyrite	35.40	30.53	33.51	0.00	0.00	0.00	1.32	0.00		100.76
TPH120-4A-42	Core	II	chalcopyrite	35.78	30.78	33.59	0.03	0.00	0.01	1.22	0.01		101.42
TPH120-4A-19	Core **	II	stannite	29.79	12.53	28.41	0.07	0.08	0.00	0.92	0.000	27.86	99.66
TPH120-4A-22	Core **	II	sphalerite	33.82	8.15	0.06	0.00	0.03	0.02	57.27	0.006	0.00	99.36

1325

1326

1327

Note: \* - located within cataclastic band and close to stylolite. \*\* - located along stylolite

Sphalerite and stannite compositions from locations indicated by \*\* have been used to calculate the temperatures of sphalerite-stannite equilibrium following the geothermometer of Shimizu and Shikazono (1985). See text for more explanations.

1328

